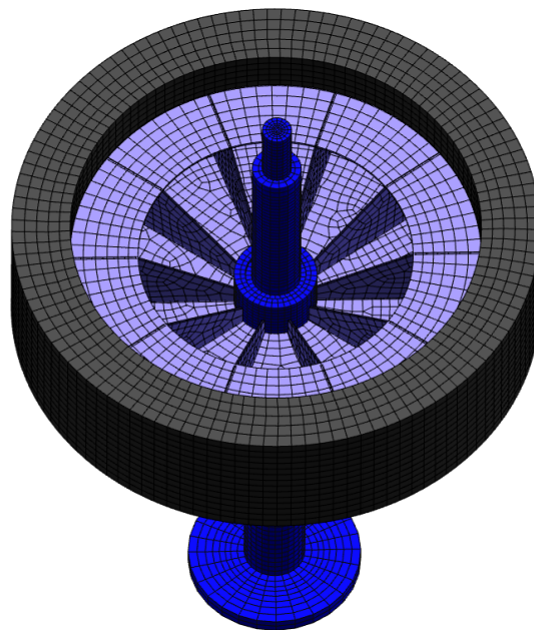# Rotor Dynamic Modeling of Hydropower Rotors by 3D-Finite Element Analysis

Simon Pääjärvi

Mechanical Engineering, master's level
2022

Luleå University of Technology
Department of Engineering Sciences and Mathematics

Acknowledgements

Abstract

By using the rotor dynamic capabilities of Simcenter Nastran Rotordynamics, an eigenvalue analysis of 3D-finite element models of the Jeffcott rotor and the overhung rotor were conducted and compared to the results with beam-based, lumped parameter models. The first two critical speeds of the Jeffcott rotor were estimated with variations of 3.9 and 6.4%. The first three critical speeds of the overhung rotor were estimated with 8.5, 6.7 and 6.5% variations, respectively. The Jeffcott rotor was also analysed with different element configurations: Solid elements, axisymmetric Fourier elements, beam/solids and all beam elements. The Fourier elements were the most appropriate option for axisymmetric rotors regarding computational time and accuracy.

Tilting pad journal bearings were simulated and validated against data from Vattenfall's facilities in Älvkarleby, where a vertical rotor is connected to two four-pad tilting pad journal bearings. The bearing formulation was defined in a Fortran based subroutine, which acquires the rotor's speed and position to supply a bearing load vector in Simcenter Nastran's transient solver. The experimental rig was also modelled to include the rotor/stator interaction. The force and displacement orbits at the bearings were replicated adequately concerning experimental data, where a maximum deviation of 20.8% and 9.8% were observed for the forces in x and y-directions.

A 3D-finite element model and a beam based finite element model were compared for an actual hydropower unit, which aimed to investigate the mode extraction procedure and how high mass, elastic rotor components influence the system's dynamics. Consistent rotor modes were identified at frequencies within 15% deviation, where the maximum deviation occurred in the upper range frequency pairs. Convergence between the models was observed for the static, lower range frequencies when considering a rigid generator rotor in the 3D finite element model. The outcome is consistent with the model assumptions and underlines that the beam based model cannot capture specific contributions from elastic rotor components.

3D-finite element analysis is a viable option when considering non-axisymmetric and complex rotors. High mass, non-rigid components must be analysed in this manner as their dynamic contributions may not be captured with other approaches. Intricate and non-rigid supporting structures are also suitable for 3D modelling to properly reflect the stator-rotor interaction. It is a delicate matter to pinpoint when these conditions occur, and modelling decisions must be therefore be substantiated by simulations and experimental validation.

Contents

1 Introduction

Rotating machinery serves as a fundamental component in the large-scale production of energy. Indeed, 99.6% of Sweden's energy production in 2019 can be attributed to rotating machinery, i.e. nuclear power, hydropower, wind power and combustion-based power [1]. These methods can effectively be condensed to one fundamental element, the energy transfer between a fluid and a turbine, where a generator converts the mechanical energy into electric power. Moreover, 46% of the world's energy consumption is associated with rotating machines [2].

Rotor dynamics is a branch of applied mechanics for analysing force and motion in these vastly important systems, e.g. studying vibration due to misalignment or mass imbalance. It provides the theoretical framework for analysing these phenomena, which can interfere with function and performance, resulting in malfunction and catastrophic failures [3].

1.1 Background

Rotor dynamic modelling can utilise varying approaches. Elementary rotor dynamic models merely consist of lumped masses supported by elastic and viscous elements, which nevertheless can capture critical phenomena such as the gyroscopic effect. Different methods for the modelling of a rotor assembly are given in Figure 1, which showcases a simple, axisymmetric rotor assembly discretised by two different approaches. The rotor assembly encompasses the rotor, its connections to the supporting structure (e.g. the bearings) and the supporting structure itself. All approaches condense into a mathematical model, here represented by the equation of motion.
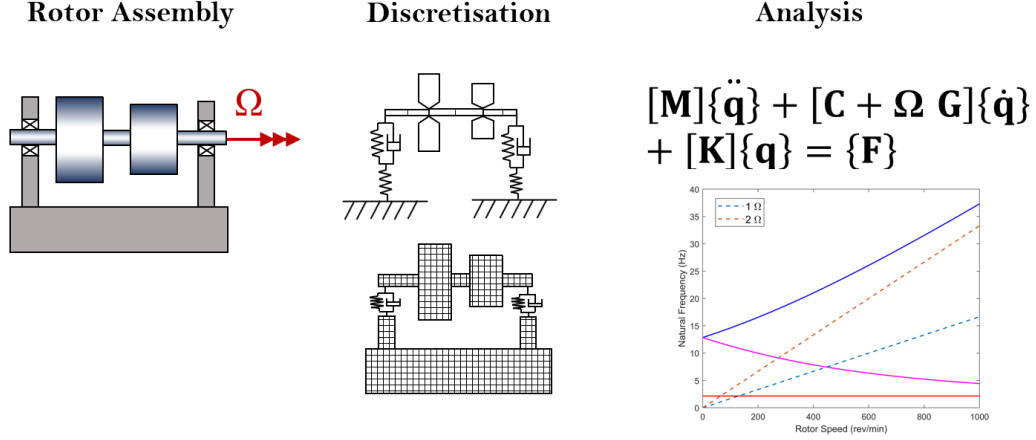
Figure 1: Different idealisation approaches in the spectrum for rotor dynamical modelling, e.g. beam based lumped parameter models and full-scaled 3D-FEM models, where the supporting structure is also discretised.

The need for advanced modelling methods arises with the system's increasing complexity. Beam based finite element models suffice if all nodes are positioned on the axis of rotation and when rotor disks are treated as purely inertial contributions, but fail to consider when a cross-section of the rotor deforms significantly, both in and out of the plane [4]. Furthermore, complex and irregular rotor geometries are problematic to model sufficiently. Several rotor components cannot be treated as rigid bodies and require further considerations. To obtain an accurate overview of the dynamics of a rotor assembly, the supporting structure may also need to be taken into account with a high level of detail, which makes 3D modelling an intriguing alternative. Nevertheless, the method is associated with high computational complexity and inscrutable results, as the resulting systems tend to exhibit high levels of freedom.

1.2   Thesis Objectives

The thesis aims to identify when 3D-finite element analysis is a viable option in rotor dynamic analysis. More specifically, to conclude when the benefits exceed the potential costs of the modelling approach. The following five objectives aim to provide the necessary insights.

⬦ Evaluate methods for implementing user-written bearing models

⬦ Analyse if/how significant rotor modes are extracted in the analysis of highly discretised 3D-models

⬦ Evaluate possibilities for combining stationary and rotating structures

⬦ Pinpoint appropriate element type combinations

⬦ Determine suitable rotor components for 3D-finite element analysis

2   Theory

The theoretical framework of the thesis is presented below.

2.1   The Generalized Eigenvalue Problem in State Vector Formulation

Consider the equation of motion for the free response of a general rotor assembly, where both gyroscopic and damping matrices are included

$$\mathbf{M}\ddot{\mathbf{q}} + (\mathbf{C} + \Omega\mathbf{G})\dot{\mathbf{q}} + \mathbf{K}\mathbf{q} = \mathbf{0}. \tag{1}$$

$\mathbf{M}$ is the inertial matrix, $\mathbf{C}$ the damping matrix, $\mathbf{G}$ the gyroscopic matrix, $\mathbf{K}$ the stiffness matrix and Ω the angular velocity of the rotor. The state-vector is defined as $\mathbf{r}^T = \{\mathbf{q}^T, \dot{\mathbf{q}}^T\}$. Thus, the equations of motion may be reformulated as the following system of first-order differential equations [5]

$$\mathbf{S}\dot{\mathbf{r}} + \mathbf{R}\mathbf{r} = \mathbf{0}. \tag{2}$$

The composite matrices in Equation (2) are

$$\mathbf{S} = - \begin{bmatrix} \mathbf{I} & \mathbf{0} \\ \mathbf{0} & \mathbf{M} \end{bmatrix}, \quad \mathbf{R} = \begin{bmatrix} \mathbf{0} & -\mathbf{I} \\ \mathbf{K} & \mathbf{C} + \Omega\mathbf{G} \end{bmatrix}. \tag{3}$$

Assume harmonic solutions on the form $\mathbf{r} = \mathbf{v}e^{-\lambda t}$, which yields the following equation

$$(\mathbf{R} - \lambda\mathbf{S})\mathbf{v} = \mathbf{0}. \tag{4}$$

Let $\mathbf{A} = \mathbf{S}^{-1}\mathbf{R}$. The general eigenvalue problem is now explicitly formulated, obtaining

$$(\mathbf{A} - \lambda\mathbf{I})\mathbf{v} = \mathbf{0}, \tag{5}$$

where λ is the eigenvalue and $\mathbf{v}$ its corresponding eigenvector.

2.2   Particular Solution in State Vector Formulation

By adding a harmonic excitation to Equation (2) compromised of both sine and cosine contributions, the following equation of motion is formulated

$$\mathbf{S}\dot{\mathbf{r}} + \mathbf{R}\mathbf{r} = \mathbf{f_s}\sin(\Omega t) + \mathbf{f_c}\cos(\Omega t), \tag{6}$$

where Ω denotes the driving/exciting frequency. It is now reasonable to assume a harmonic, particular solution on form $\mathbf{r_p} = \mathbf{a}\sin(\Omega t) + \mathbf{b}\cos(\Omega t)$, which yields

$$-\Omega\mathbf{S}\left(\mathbf{a}\cos(\Omega t) - \mathbf{b}\sin(\Omega t)\right) + \mathbf{R}(\mathbf{a}\sin(\Omega t) + \mathbf{b}\cos(\Omega t)) = \mathbf{f_s}\sin(\Omega t) + \mathbf{f_c}\cos(\Omega t). \tag{7}$$

By collecting the sine and cosine terms into two separate equations, the following equations can be formulated

$$\Omega\mathbf{S}\mathbf{b} + \mathbf{R}\mathbf{a} = \mathbf{f_s} \tag{8}$$

$$-\Omega\mathbf{S}\mathbf{a} + \mathbf{R}\mathbf{b} = \mathbf{f_c}. \tag{9}$$

The equation system below is now solved for amplitudes $\mathbf{a}$ and $\mathbf{b}$ as

$$\begin{Bmatrix} \mathbf{a} \\ \mathbf{b} \end{Bmatrix} = \begin{bmatrix} \mathbf{R} & \Omega\mathbf{S} \\ -\Omega\mathbf{S} & \mathbf{R} \end{bmatrix}^{-1} \begin{Bmatrix} \mathbf{f_s} \\ \mathbf{f_c} \end{Bmatrix}. \tag{10}$$

The norm of these amplitudes can be analysed for various values of the rotor speed to obtain a frequency response function. Notice that invertibility is assumed for the composite matrix in Equation (10).

2.3 The Jeffcott Rotor

Consider the Jeffcott rotor in Figure 2. The rotor is equipped with a circular disk, represented by the lumped mass m, the diametral moment of inertia J_d (about the x and y-axis) and the polar moment inertia J_p (around the z-axis). The rotor rotates with a constant speed Ω. The length of the rotor is denoted ℓ, which is the sum of lengths a and b. The shafts exhibit the area moment of inertia I and add negligible inertial contributions to the system. Isotropic elastic material with Young's modulus E and density ρ is assumed. All translations are fixed at the rotor supports, located at the left and right ends.
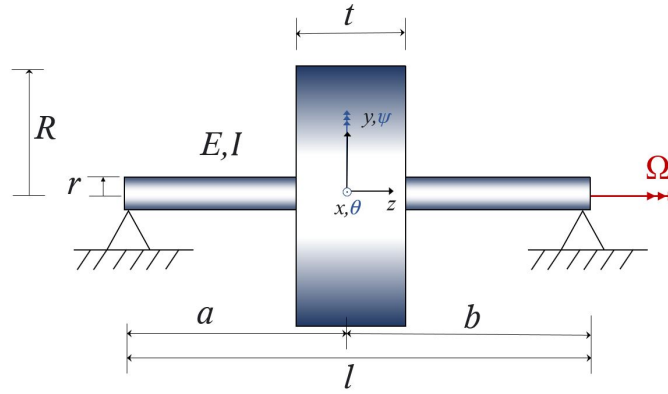
Figure 2: The Jeffcott rotor.

For an undamped rotor without the influence of external forces, the equations of motion of the rotor can be formulated [6]

$$\mathbf{M\ddot{q}} + \Omega\mathbf{G\dot{q}} + \mathbf{Kq} = \mathbf{0}, \tag{11}$$

where $\mathbf{q} = \left\{x, y, \theta, \psi\right\}^T$ is a vector consisting of the disk displacements, as indicated by Figure 2. $\mathbf{M}$ is the inertial or mass matrix of the system, $\mathbf{K}$ is the stiffness matrix and $\mathbf{G}$ is the gyroscopic matrix.

The Jeffcott rotor exhibits unconstrained rotational degrees of freedom at the pinned supports. However, for a static reduced system where the disk's degrees of freedom are the master degrees of freedom, the matrices are as follows [7]

$$
\mathbf{M} = \begin{bmatrix} m & 0 & 0 & 0 \\ 0 & m & 0 & 0 \\ 0 & 0 & J_d & 0 \\ 0 & 0 & 0 & J_d \end{bmatrix},
\tag{12}
$$

$$
\mathbf{G} = \begin{bmatrix} 0 & 0 & 0 & 0 \\ 0 & 0 & 0 & 0 \\ 0 & 0 & 0 & J_p \\ 0 & 0 & -J_p & 0 \end{bmatrix},
\tag{13}
$$

and

$$
\mathbf{K} = \begin{bmatrix} k_{xx} & 0 & 0 & k_{x\psi} \\ 0 & k_{yy} & -k_{y\theta} & 0 \\ 0 & -k_{\theta y} & k_{\theta\theta} & 0 \\ k_{\psi x} & 0 & 0 & k_{\psi\psi} \end{bmatrix}.
\tag{14}
$$

The stiffness matrix is also symmetrical, i.e. $k_{x\psi} = k_{\psi x}$ and $k_{y\theta} = k_{\theta y}$. The stiffness coefficients of the isotropic shaft is obtained from elementary beam theory [7]

$$
k_{xx} = k_{yy} = 3EI\left(\frac{a^3 + b^3}{a^3 b^3}\right)
\tag{15}
$$

$$
k_{\theta\theta} = k_{\psi\psi} = 3EI\left(\frac{a + b}{ab}\right)
\tag{16}
$$

$$
k_{x\psi} = k_{y\theta} = 3EI\left(\frac{a^2 - b^2}{a^2 b^2}\right).
\tag{17}
$$

Considering the midspan rotor, i.e. $a = b = \frac{l}{2}$, results in

$$k_{xx} = k_{yy} = \frac{48EI}{\ell^3} \tag{18}$$

$$k_{\theta\theta} = k_{\psi\psi} = \frac{12EI}{\ell} \tag{19}$$

$$k_{x\psi} = k_{y\theta} = 0. \tag{20}$$

Due to the symmetry, the stiffness matrix is now uncoupled, i.e. its non-zero elements are placed on the diagonal. The disk mass and inertia, along with the shaft's area moment of inertia, are expressed as the following set of equations, written as functions of the rotor geometry [8].

$$m = \rho\pi t R^2, \tag{21}$$

$$J_d = \frac{1}{4}mR^2 + \frac{1}{12}mt^2, \tag{22}$$

$$J_p = \frac{1}{2}mR^2, \tag{23}$$

$$I = \frac{1}{2}mr^4. \tag{24}$$

2.4 The Overhung Rotor

Consider the overhung rotor depicted in Figure 3. The rotor is equipped with a circular disk at its right end, represented by mass m, diametral moment of inertia J_d and polar moment of inertia J_p. The shaft has the area moment of inertia I and add no inertial contributions to the system. The rotor length is denoted ℓ. Isotropic linear-elastic material with Young's modulus E and density ρ is assumed.
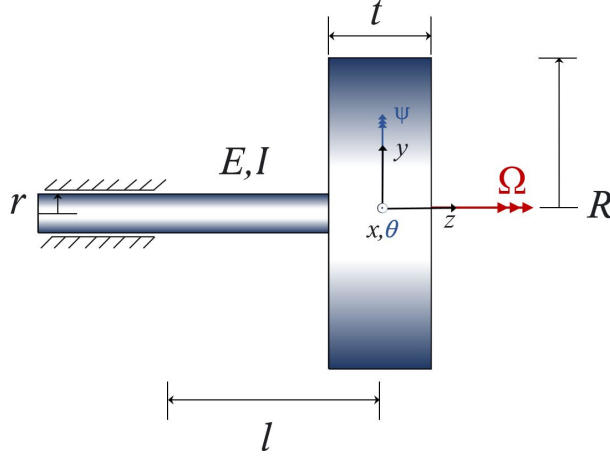
Figure 3: The overhung rotor.

All translations and rotations are fixed on the left side of the rotor. For an undamped and unforced rotor, the equations of motion of the rotor can be written as presented in Equation (11), where $\mathbf{q} = \left\{ x, y, \theta, \psi \right\}^T$ is a vector consisting of the disk displacements, with directions illustrated in Figure 3. Mass, gyroscopic and stiffness matrices follow the same convention as in in Equations (12) to (14), albeit with different stiffness matrix coefficients, once again obtained from elementary beam theory as [7]

$$k_{xx} = k_{yy} = \frac{12EI}{l^3}, \tag{25}$$

$$k_{\theta\theta} = k_{\psi\psi} = \frac{4EI}{l}, \tag{26}$$

$$k_{x\psi} = k_{y\theta} = \frac{6EI}{l^2}. \tag{27}$$

Similarly, the disk's inertial and geometrical properties m, J_d, J_p and I are given as in Equations (21) to (24), expressed as functions of the rotor's geometry.

9

2.5 Tilting Pad Journal Bearings

Figure 4 illustrates a tilting four-pad journal bearing and a rotor. The rotor is radially displaced with the distance e from the bearing's geometrical centre and rotates with constant speed Ω. The radial clearance is the distance between the geometrical centre of the rotor and the geometrical centre of the bearing and is denoted Δr. Two separate coordinate systems are shown, the (ξ, η)-coordinate system, which follows the rotor's angular position α, and a stationary (x, y)-system.
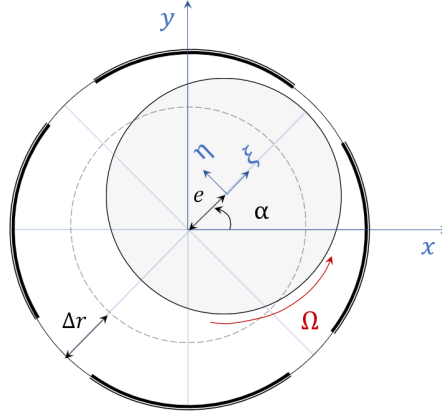
Figure 4: An illustration of a four-pad tilting bearing showcasing the stationary and rotating coordinate systems.

The entries of the local bearing stiffness matrix, $\mathbf{K}_\beta$ and the local bearing damping matrix $\mathbf{C}_\beta$ in the rotating (ξ, η)-coordinate system are given as

$$\mathbf{K}_\beta = \begin{bmatrix} K_{\xi\xi} & K_{\xi\eta} \\ K_{\eta\xi} & K_{\eta\eta} \end{bmatrix} \tag{28}$$

and

$$\mathbf{C}_\beta = \begin{bmatrix} C_{\xi\xi} & C_{\xi\eta} \\ C_{\eta\xi} & C_{\eta\eta} \end{bmatrix}. \tag{29}$$

The following transformation enables the transition between the two coordinate systems

$$\mathbf{K_B} = \mathbf{T^T K_\beta T} \tag{30}$$
$$\mathbf{C_B} = \mathbf{T^T C_\beta T}, \tag{31}$$

10

where the transformation matrix $\mathbf{T}$ is

$$\mathbf{T} = \begin{bmatrix} \cos(\alpha) & -\sin(\alpha) \\ \sin(\alpha) & \cos(\alpha) \end{bmatrix}. \tag{32}$$

Upon transforming the matrices to the stationary coordinate system, the bearing load vector is formulated as the sum of displacement and velocity dependent forces

$$\mathbf{f} = \mathbf{K_B}\mathbf{u} + \mathbf{C_B}\dot{\mathbf{u}}, \tag{33}$$

where $\mathbf{u} = \{x, y\}^T$ is the vector of bearing displacements.

The entries of the stiffness and damping in the rotating coordinate system are functions of eccentricity ratio ε, the rotor speed Ω and angular position α. The following set of functions gives the entries [9]

$$K_{ij} = \frac{K_{ij}^{max}(\Omega, \varepsilon) + K_{ij}^{min}(\Omega, \varepsilon)}{2} + \mathcal{H}(\alpha) \cdot \frac{K_{ij}^{max}(\Omega, \varepsilon) - K_{ij}^{min}(\Omega, \varepsilon)}{2} \tag{34}$$

$$C_{ij} = \frac{C_{ij}^{max}(\Omega, \varepsilon) + C_{ij}^{min}(\Omega, \varepsilon)}{2} + \mathcal{H}(\alpha) \cdot \frac{C_{ij}^{max}(\Omega, \varepsilon) - C_{ij}^{min}(\Omega, \varepsilon)}{2}. \tag{35}$$

Notice that the equations above can be interpreted as the sum of a mean stiffness (the first term) and a deviatoric part (second term) multiplied with a harmonic contribution. The harmonic coefficient, $\mathcal{H}$, is defined as

$$\mathcal{H} = \begin{cases} \cos(n\alpha) & i = j = \xi \\ -\cos(n\alpha) & i = j = \eta \\ -\sin(n\alpha) & i \neq j \end{cases}, \tag{36}$$

where n is the number of pads in the bearing. The eccentricity and rotor angle (see Figure 4 for illustration) can be computed in the stationary coordinate system. The ratio of eccentricity is defined as the ratio between eccentricity and the radial clearance. The angular position is computed from the rotor's position in the cartesian coordinate system. Thus,

$$\alpha = \text{atan2}(x, y) \tag{37}$$

$$\varepsilon = \frac{e}{\Delta r} = \frac{\sqrt{x^2 + y^2}}{\Delta r}. \tag{38}$$

11

The atan2-function extends the traditional arctan-function available in FORTRAN language, [10] which outputs an angle in the range of $(-\pi/2, \pi/2)$. Hence, ambiguity occurs when determining the angular positions in the second and third quadrants. The complete extension can be formulated as

$$\text{atan2}(x, y) = \begin{cases} \arctan(y/x) & \text{if } x > 0, \\ \pi/2 - \arctan(y/x) & \text{if } y > 0, \\ -\pi/2 - \arctan(y/x) & \text{if } y < 0, \\ \arctan(y/x) \pm \pi & \text{if } x < 0, \\ \text{undef} & \text{if } x = y = 0. \end{cases} \tag{39}$$

This function outputs an unambiguous angle in the range of $(-\pi, \pi]$, effectively covering all four quadrants.

2.6 Unbalanced Magnetic Pull

Due to unavoidable asymmetries in the air gap between the rotor and stator of an electric generator, considerable radial attraction forces arise, contributing to reduced stiffness of the rotor assembly. Consider a rotor spider connected to a shaft acted upon magnetic force and moment due to this interaction. The connection is offset by the distance ℓ to the centre of the rotor rim where the magnetic force acts. The rotor rim length is denoted h. By considering small eccentricities, i.e. $\varepsilon \leq 0.1$, by definition given in Equation (38), the following stiffness matrix can be formulated, yielding a constant and linear relationship between forces and displacements [11]

$$\mathbf{K_{MAG}} = k_m \begin{bmatrix} 1 & 0 & 0 & \ell \\ 0 & 1 & -\ell & 0 \\ 0 & -\ell & \Gamma & 0 \\ \ell & 0 & 0 & \Gamma \end{bmatrix}, \tag{40}$$

where

$$\Gamma = \frac{1}{3h} \left(\left(\frac{h}{2} + l \right)^3 + \left(\frac{h}{2} - l \right)^3 \right) \tag{41}$$

The matrix in Equation (40) describes the linear force/displacement relation acting at a node with two translational and two rotational degrees of freedom. k_m is the scalar magnetic stiffness, approximated by the following relation

12

$$k_m = \frac{\mu_0 S_s^2 r_s^3 h \pi}{2p^2 \Delta r^2}, \tag{42}$$

where p is the number of pole pairs, S_s is the stator's linear current density, and μ_0 is the permeability of free space. Δr denotes the air gap, i.e. the difference between the rotor's outer diameter and the stator's inner diameter, here represented as r_s.

3 Methods

This section represents applied methods and concepts in the thesis.

3.1 The Campbell Diagram

The *Campbell diagram* or *natural frequency map* provides an overview of the natural frequencies of a rotor assembly, which may vary with the angular speed of the rotor [12]. For a complex-valued eigenvalue, the imaginary contribution is the natural frequency and resides on the ordinate. The rotor speed is shown on the abscissa. A typical Campbell diagram is presented in Figure 5, exhibiting both static and speed-dependent frequencies. Furthermore, the chart may include lines corresponding to the rotor speed (1Ω) and the double rotor speed (2Ω). Where the intersection occurs, a resonance speed is reached, which is denoted as a *critical speed*.
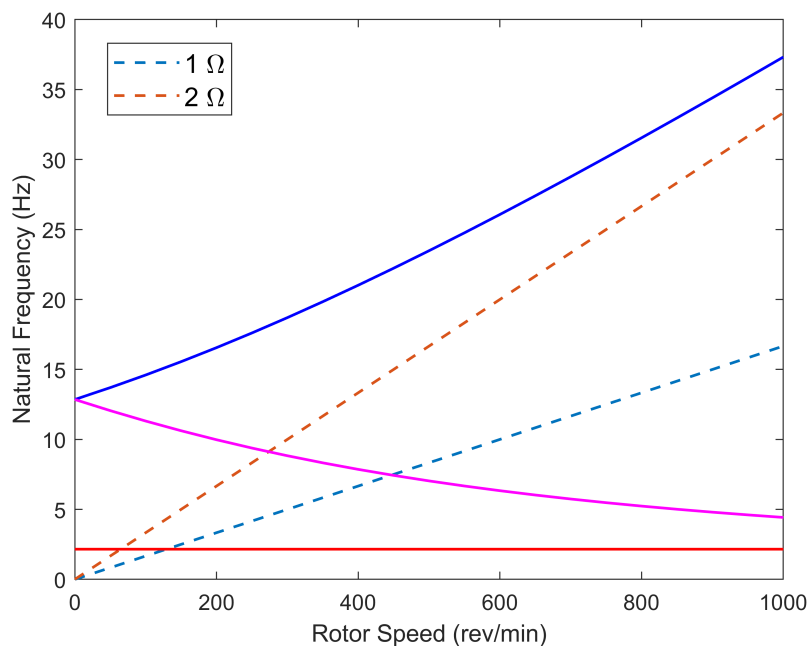

Figure 5: A typical Campbell diagram that illustrates both stationary and speed-dependent natural frequencies.

3.2   Simcenter Nastran Rotor Dynamics

As of the Simcenter Nastran 2022 1.1 release, the rotor dynamic analysis is collected under SOL 414 Rotor Dynamics. This encompasses the following solution types [13].

- MANOUVERS (110)

  Linear static analysis concerning gyroscopic forces.

- EIGENVALUES AND SUPER ELEMENT REDUCTION (414/103)

  Computation of eigenvalues for a static rotor. It offers the creation of super elements, which use the original rotor's boundary nodes to create a condensated element that can be represented by mass, stiffness and gyroscopic matrices.

- COMPLEX MODAL (414/110)

  Analyses the system for different rotor speeds. Used to produce Campbell diagrams, compute mode shapes, compute damping ratios and determine critical speeds.

- HARMONIC RESPONSE (414/111)

  Frequency response analysis with both synchronous and asynchronous options. Mass imbalance and geometric misalignment can be implemented.

- TRANSIENT RESPONSE (414/129)

  Time-dependent analysis, e.g. for accelerating rotors and time-dependent loads.

The thesis will conduct analysis in solver 414/110 (Complex Modal), 414/111 (Harmonic Response) and SOL 414/129 (Transient Response).

3.3 Implementation of Custom Bearing Formulations in Simcenter Nastran

User-written bearing functions may be included in Simcenter Nastran Rotor Dynamics [14]. The procedure is illustrated in Figure 6. The equations describing bearing forces are defined in the source file, a .f-file written in FORTRAN-programming language. The source file is formatted as a FORTRAN subroutine, with inputs and outputs defined as the arguments. An example of a .f-file used for the transient simulations is given in Appendix A: Switch Routine Code.

Figure 6: The procedure for custom bearing implementation. **1)** Define switch routine in the source file, which includes the bearing equations defined as a load vector, **2)** Compile the system .dll-file with the assistance of a local FORTRAN-compiler. **3)** Solve the model in Simcenter Nastran. The switch routine is called during each iteration by the solver, and requested variables are returned.

The compilation is done in the following steps for a Microsoft Windows operating system using the command prompt. The outlined steps must be executed from top to bottom.

- Set the SAM_COMPILER variable to the location of the FORTRAN-compiler bin.

- Create the user environment variable (SAM_USERDLL). Set the location as the complete path to the user-written .dll-file.

- Set the SAM_EXE variable to the complete path where Simcenter Samcef is installed

- In the command prompt, navigate to the directory where the user-written .dll-file resides. Write "%SAM_EXE%\samcef.cmd" dll" to initiate compilation.

For example, the following three lines in the command prompt will compile the .dll-file. CodeBlocks is the integrated developer environment with the accompanying GNU Fortran compiler.

SET SAM_COMPILER = C: \PROGRAM FILES\CODEBLOCKS \MINGW

SET SAM_EXE = C: \PROGRAM \SIEMENS \NX2007 \NXNASTRAN \SCNAS \EM64TNTL \SAMCEF

"%SAM_EXE% \SAMCEF.CMD" DLL

The user must navigate to the location of the .dll-file in the command prompt. The compilation shall be repeated for any modifications in the source file code. Only the second step must be considered for the general usage of the bearing function.

3.4   Element Connections

An illustration of a bearing connection in Simcenter Nastran Rotordynamics is shown in Figure 7. The rotor is connected to a stator by a CBEAR2-element, which may use nodal displacement, velocity and acceleration as input data for force generation. Notice that the nodes connected by the bearing element are coincident; the distance (blue line) is purely for illustration. Multi-point constraint (MPC) elements connect the concurrent node to the nodes of the rotating and stationary components. The coincident bearing nodes are chosen as the independent nodes for the RBE2-elements, which act as a rigid connection. Thus, any movement at the independent node (e.g. the rotation) is transmitted to the dependent nodes of the rotor. The user shall be aware that the inclusion of the RBE2 element adds stiffness to the affected cross-section, as the nodes cannot exhibit any relative movement to each other.
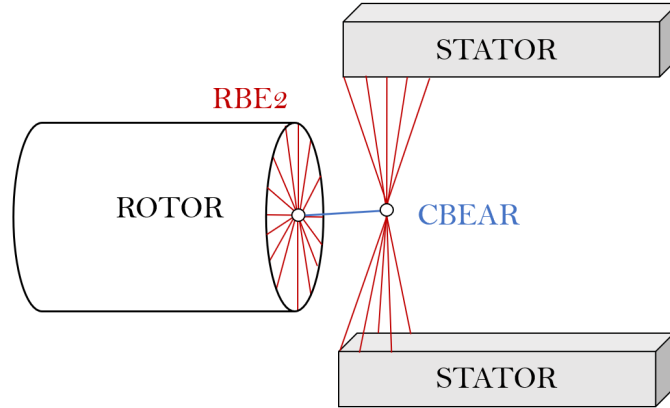
Figure 7: Illustration of a bearing connection.

Beam elements and 3D-solid elements can also be combined. However, beam elements exhibit rotational degrees of freedom, not supported by solid elements. To overcome this issue, RBE2-elements can be used. As rotations cannot be utilised, one may use translations at a fixed distance to provide a rotation. Once again, this affects the stiffness of the connected cross-section. In Figure 8, a beam element (purple) is connected to a rotor disk which is meshed with 3D-solids. The legs of the RBE2-element connect the independent node of the beam element to the dependent nodes of the solid elements, which eliminates any relative motion between the dependent nodes. Thus, a rotation of the beam node will transmit as a translation of the dependent nodes.
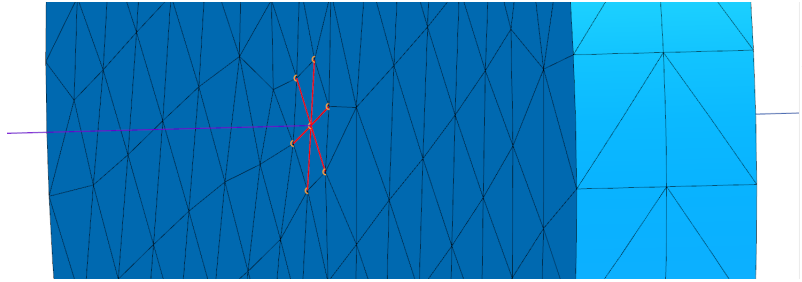

Figure 8: The connection between line element (beam) and 3D-tetrahedrons. The dependent nodes reside on the rotor disk.

3.5 Modelling Mass Unbalance

Mass unbalance may be applied to model a rotating force, which rotates coherently with the rotor speed. The load is applied on nodes that reside on the rotor's central axis, that is, the axis of rotation, see Figure 9. The unbalance load is applied by LOAD TYPE → UNBALANCE MASS in the PrePost-environment of the simulation file.

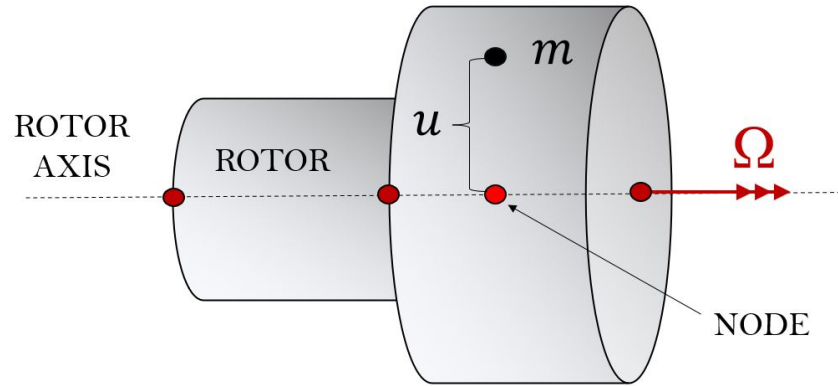**Figure 9:** Illustration for applying mass unbalance. The unbalance is used on the mid-node located on the rotor's central axis, e.g. on the mid-node of the rotor.

The mass unbalance is specified by inputting the unbalance mass and its distance from the rotor axis. An arbitrary phase can also be set. The rotating speed contribution to the unbalance force is taken into account based on the input in the ROTORD-entry.

3.6 The ROTORD Entry

The ROTORD entry is mutual for the named solvers. Drop-down options are denoted by the bullets (•), whereas numerical input is represented by the hyphens (-).

Table 1: Options for the ROTORD Entry.

Rotation Speed Variation	• Linear by Steps
	• Constant
	• Function of Sweeping Parameter
Starting Speed (RSTART)	-
Number of Steps (NUMSTEP)	-
Reference System (REFSYS)	• FIX
	• ROT
Reference and Output Units (RUNIT)	• RPM
	• HZ
Whirl Direction Thresold (ORBEPS)	-
.f06 Output (ROTPRT)	• Generalized Matrices
	• Eigenvalue Summary and Eigenvectors
	• Generalized Matrices, Eigenvalues
	and Eigenvectors
Analysis Type (SYNC)	• Asynchronous
	• Synchronous

ROTATION SPEED VARIATION provides alternatives for specifying the rotor speed, which can be declared constant or varying. The reference system is set in REFSYS, where both rotating and stationary frames are supported.

4 Results and Discussion

Results and accompanying discussion of the thesis are presented below.

4.1 Analysis of Jeffcott Rotor and Overhung Rotor

This section presents the eigenvalue analysis of the two elementary rotors introduced in Sections 2.3 and 2.4. The eigenvalue analysis is conducted in Simcenter Nastran's modal solver SOL 414/110 to determine the speed-dependent eigenmodes and eigenvalues of the rotor, which allows the identification of critical speeds. Furthermore, a harmonic response solver (SOL 414/111) is utilised to determine the synchronous response.

4.1.1 The Jeffcott Rotor

The discretised, mid-span Jeffcott rotor is shown in Figure 2. The translations at the shaft ends are fixed, representing a pinned boundary condition. The rotor is discretised with 5448 solid eight-noded hexaeder elements and the system is analysed in a stationary frame of reference.
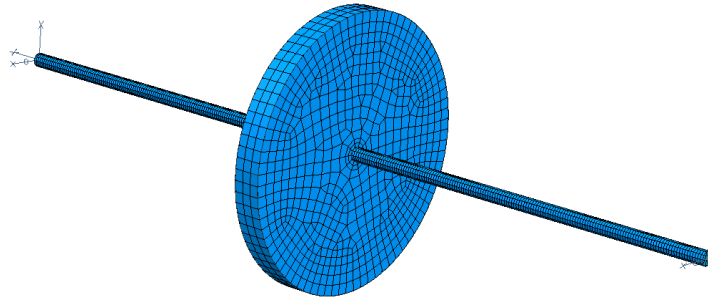
Figure 10: Jeffcott Rotor meshed with 5448 solid HEX8 elements.

21

The input data for the analysed rotor is given in Table 2. This provides the input for the matrices in the equation of motion presented in Equation (11), as well as the input to Simcenter Nastran.

Table 2: Input data for the mid-span Jeffcott rotor analysis.

Young's Modulus, E	206.94 GPa
Density, ρ	7829 kg/m^3
Disk thickness, t	0.100 m
Disk radius, R	0.0250 m
Rotor length, ℓ	3.00 m

The first two distinct eigenmodes at 0 rev/min are shown in Figure 11, visualised in Simcenter Nastran post-processing environment.
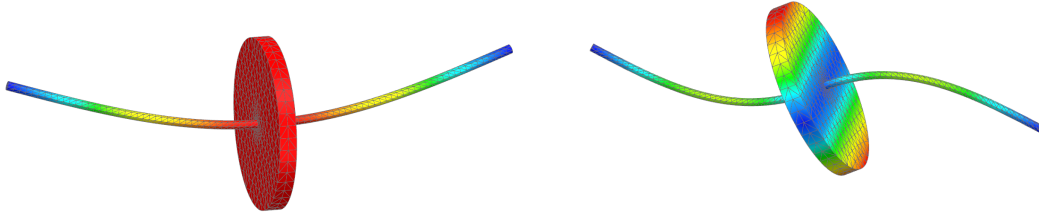
(a) Bouncing vibration mode at 2.16 Hz   (b) Tilting vibration at 12.6 Hz

Figure 11: Visualisation of the first two distinct modes of the Jeffcott Rotor.

The analytical eigenvalues are found by solving Equation (5) by the use of the eig()-command in MATLAB R2021b and serve as a comparison to the finite element results. The Campbell diagram in the range of 0-1000 rev/min is illustrated in Figure 12.
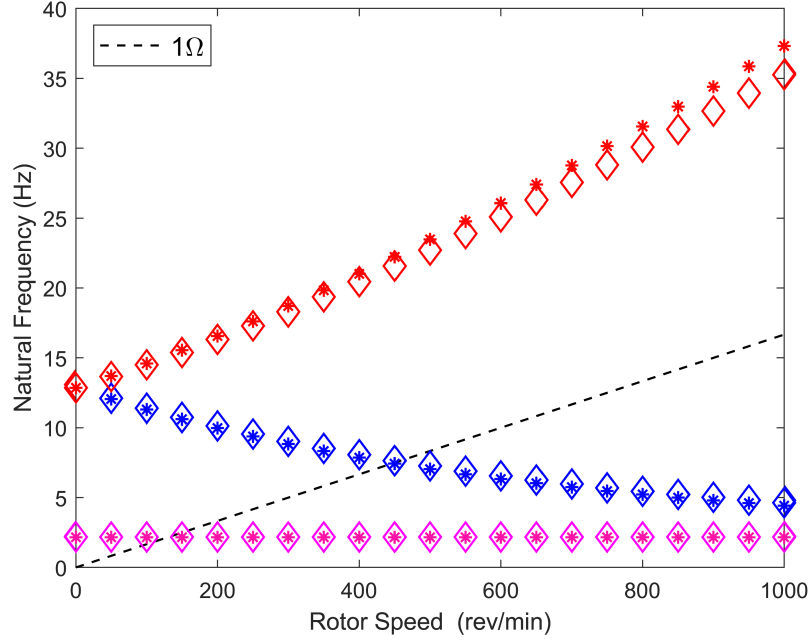
Figure 12: Campbell diagrams for the 3D-solid analysis ($\diamond$) and the analytical approach with beam elements ($*$).

The two critical speeds first critical speeds for both approaches are given in Table 3, showcasing a deviation of 3.9 % and 6.38 % between the analytical solution and the 3D-finite element solution.

Table 3: The first two critical speeds for the eigenvalue analysis of the Jeffcott Rotor.

	Lumped parameter	3D-FEA
Critical Speed 1 (rev/min)	130	125
Critical Speed 2 (rev/min)	447	470

The frequency response functions of the lumped parameter model and the 3D-FEA are illustrated in Figure 13 to show the frequency response of the first critical speed

23

that occurs at approximately 130 rev/min. The frequency response of the analytical Jeffcott rotor is computed by Equation (10), with an unbalanced mass of 615 kg and eccentricity of 1 mm. The unbalance force vectors are $\mathbf{f_c} = me\Omega^2 \left\{0,0,0,0,1,0,0,0\right\}^T$ and $\mathbf{f_s} = me\Omega^2 \left\{0,0,0,0,0,1,0,0\right\}^T$, respectively, which aim to excite the forward whirling modes. A frequency range of 0-300 rev/min was used with one rev/min steps. The rotor is analysed in the fixed frame of reference with the synchronous analysis option.
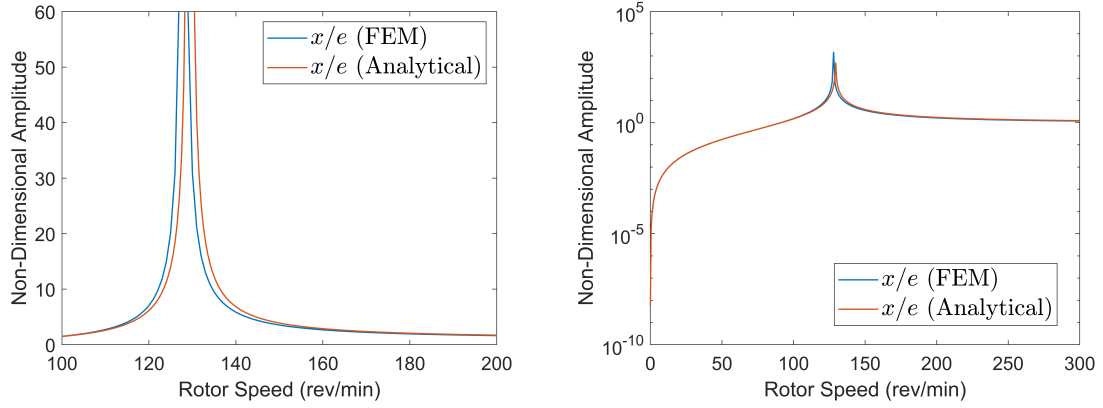
(a) Frequency response of the Jeffcott rotor, centred around the first resonance speed.

(b) Frequency response of the Jeffcott rotor with logarithmic ordinate.

Figure 13: Frequency response comparison of the Jeffcott rotor.

Both models reflect the rotor's isotropic properties and show convergence to the unbalance distance of 1 mm.

4.1.2 The Overhung Rotor

The discretised model of the overhung rotor is shown in Figure 14. The left side nodes of the shaft are fixed concerning all degrees of freedom, representing a clamped boundary condition. The rotor is discretised with 2114 solid, eight-noded hexaeder elements.
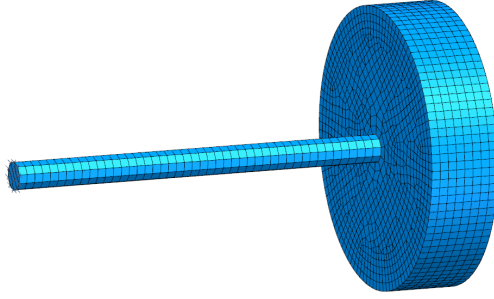
Figure 14: Overhung rotor discretised with 2114 solid HEX8 elements.

Input data for the rotor is given in Table 4 and is used as input for the matrices presented in Section 2.4.

Table 4: Input data for the overhung rotor eigenvalue analysis.

Young's Modulus, E	206.94 GPa
Density, ρ	7829 kg/m^3
Disk thickness, t	0.100 m
Disk radius, R	0.0250 m
Rotor length, ℓ	3.00 m

The first two distinct vibration modes for the stationary rotor are shown in Figure 11, visualised by the post-processing facility in Simcenter Nastran.
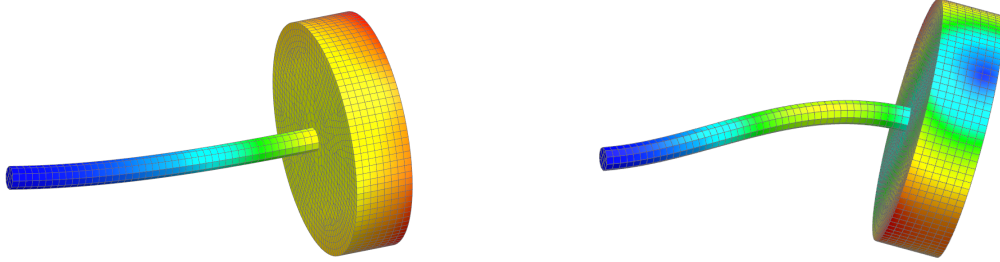
(a) Bouncing vibration mode at 1.9 Hz   (b) Tilting vibration mode at 13 Hz

Figure 15: Visualisation of the first two distinct modes of the overhung rotor.

The analytical eigenvalues are found by solving Equation (5) by the use of the eig()-command in MATLAB R2021b and serve as a comparison to the finite element result. The Campbell diagram in the speed range of 0-1000 rev/min is illustrated in Figure 12.
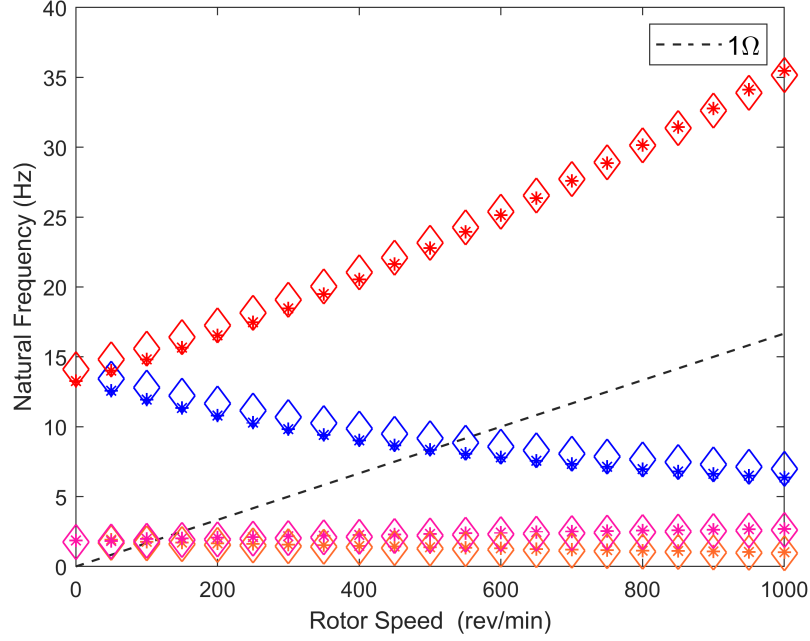
Figure 16: Campbell diagram for the solid element analysis (◇) and the analytical approach (∗).

The first three critical speeds for both approaches are given in Table 5. The deviation between the models for the three critical speeds is 8.5 %, 6.7 % and 6.5 %, respectively.

Table 5: The first three critical speeds for the eigenvalue analysis of the overhung rotor.

	Analytical	3D-FEA
Critical Speed 1 (rev/min)	106	98
Critical Speed 2 (rev/min)	119	111
Critical Speed 3 (rev/min)	501	536

The frequency response functions of the lumped parameter model and the 3D-FE model are illustrated in Figure 17, showing the frequency response of the forward whirling critical speed that occurs at approximately 105 rev/min. The frequency response of the analytical overhung rotor is computed by Equation (10), with force vectors $\mathbf{f_c} = me\Omega^2 \left\{0, 0, 0, 0, 1, 0, 0, 0\right\}^T$ and $\mathbf{f_s} = me\Omega^2 \left\{0, 0, 0, 0, 0, 1, 0, 0\right\}^T$, with a mass of 12300 kg and eccentricity 1 mm. A speed range of 0-300 rev/min was used

27

with one rev/min steps for the 3D-FEA response analysis. The rotor is analysed in the fixed frame of reference with the synchronous analysis option.
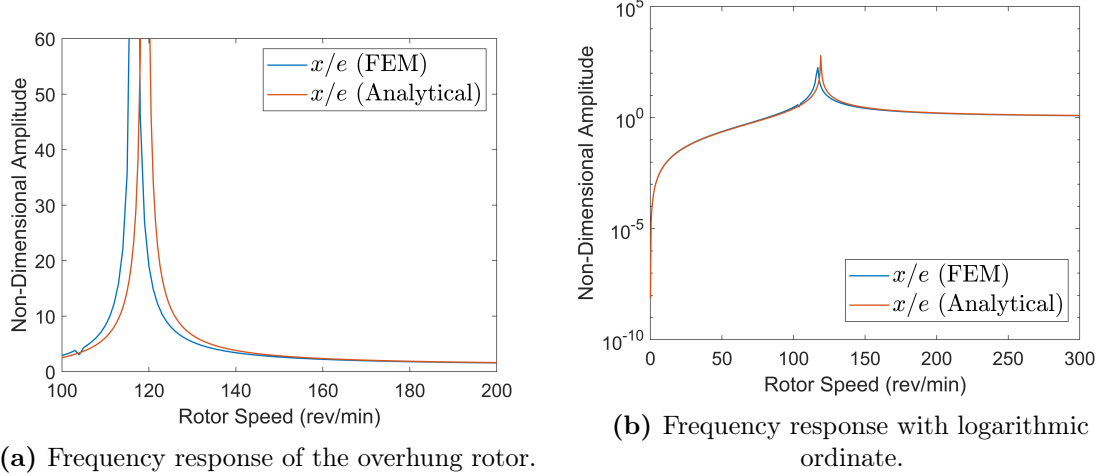

(a) Frequency response of the overhung rotor.

(b) Frequency response with logarithmic ordinate.

Figure 17: Comparison of frequency response functions between the 3D-FE model and the analytical model.

The displacement peaks occur at the critical speeds presented in Table 5. Both models catch the rotor's isotropic properties and show convergence to the unbalance distance of 1 mm. The deviation between maximum amplitudes is possibly due to numerical issues arising as both models are undamped.

The 3D-finite element results are within 10% of the analytical results for both rotors. However, it must be noted that the analytical results are by no means an ideal reference - several assumptions have been taken which may not be strictly fulfilled. E.g., the premise that the shaft provides no inertial contributions and that the disk is perfectly rigid. The mode shapes and characteristics correspond to the analytical predictions. It is noted that the gyroscopic effect is not represented identically for both models. The deviation of the speed-dependent eigenvalues tends to drift further away with higher rotor speed, suggesting different representations of the polar moment of inertia. This deviation is especially apparent for the overhung rotor.

4.2   Comparison of Element Types

The Jeffcott rotor presented in Section 2.3 is analysed for different element configurations: Solid elements, line elements, 2D-axisymmetric Fourier elements and a combination of line and solid elements. The four different discretised rotors are shown in Figure 18. The input data of the Jeffcott rotor is provided in Table 2. The eigenvalue analysis was conducted in Simcenter Nastran modal solver SOL 414/110 to determine the speed-dependent eigenmodes and eigenvalues, enabling the identification of critical speeds. These critical speeds are after that compared to the results from the analytical model in Section 4.1, which acts as a reference.

(a) Line elements.

(b) Axisymmetric Fourier-elements

(c) Solid + line elements

(d) Solid elements
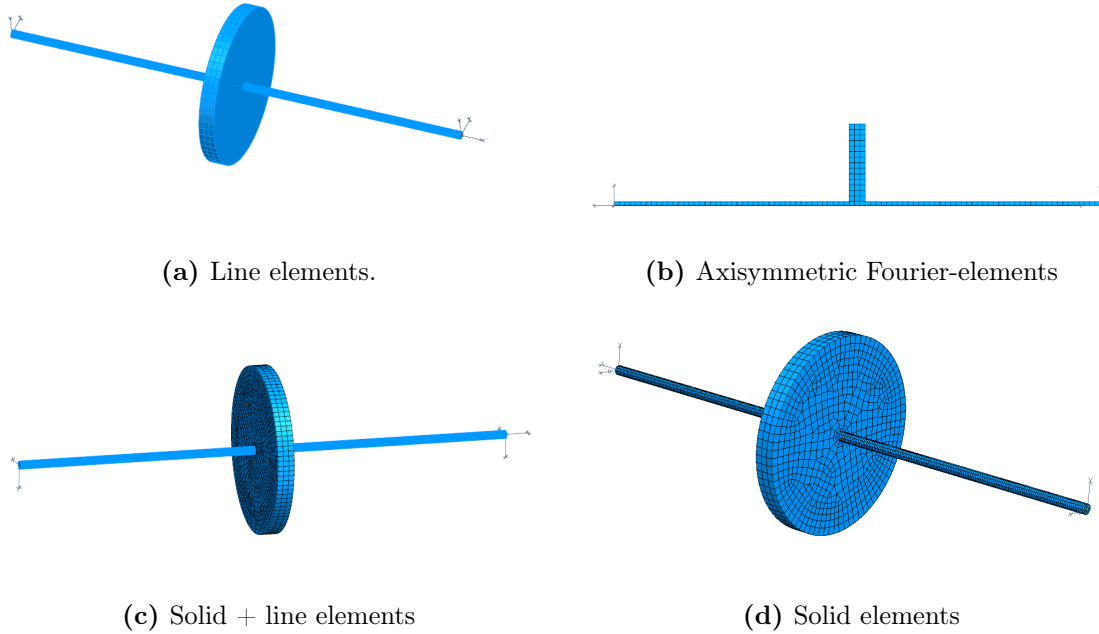
Figure 18: Different discretisation approaches for the Jeffcott rotor.

Twenty modes per rotor speed were requested for all simulations. Five beams (CBEAM) per side were utilised for the beam model, with three elements through the disk thickness. Three elements were used throughout the disk thickness and three throughout the shaft thickness for the solid and axisymmetric elements. Eight noded hexaeder (HEXA8) elements were utilised for the solids and eight noded shells (CQUADX8) for the axisymmetric model. To connect the solid element to the line elements - which lacks compatibility due to the absence of rotational degrees of

29

freedom in the solid element - an RBE2 multi-point constraint was used, connecting the (independent) centre node of the beam element to the (dependent) nodes on the disk, placed on a radius corresponding to the shaft's radial dimension.

The results from the estimation of the two first critical speeds in the 0-1000 rev/min range are given in Table 6. The deviation from the results obtained from the analysis of the Jeffcott rotor in Section 4.1 is also given (130 and 447 rev/min, respectively), along with the computational time reported from the solver. The solver identified the correct whirl direction for all element types.

Table 6: Results from the comparison between element types for the critical speed analysis.

	HEXA8	CQUADX8	CBEAM/HEXA8	CBEAM
Cr. Speed 1 (rev/min)	125	132	134	136
Cr. Speed 2 (rev/min)	470	460	465	475
Deviation (Cr. Speed 1) (%)	3.8	1.5	3.1	4.6
Deviation (Cr. Speed 2) (%)	5.1	2.9	4.0	6.3
Computational Time (s)	12.86	6.36	6	0.14

The critical speeds are found within a tolerance of 6.5% for all element types. However, it must be noted that no convergence study for the discretisation was used. Thus, it cannot be ruled out that further discretisation could provide reduced deviations. Nevertheless, the reference discretisation limit of three elements throughout the disk and two throughout the shaft was used to obtain an overview of the effect of the chosen elements. The solid elements provide the highest computational effort. The use of beam elements for the shafts halves the computational effort. The axisymmetric elements provide the slightest deviation with more than a split computational time to the full-solid option. Finally, the rotor discretised with only beam elements provides the lowest computational time, albeit with increased deviation compared to the other alternatives.

4.3   Simulation of Tilting Pad Journal Bearings

To identify possibilities for implementing custom bearing formulations in Simcenter Nastran, the non-linear bearing properties of tilting pad journal bearings were chosen as a basis for validation. Experiments from Vattenfall's rotor rig in Älvkarleby were used for comparison, encompassing data from four and eight pad tilting bearings [9]. Furthermore, the possibility of including the whole stationary structure was also researched. The rig is illustrated in Figure 19, albeit with a different rotor than the one used for the tilting pad measurements.
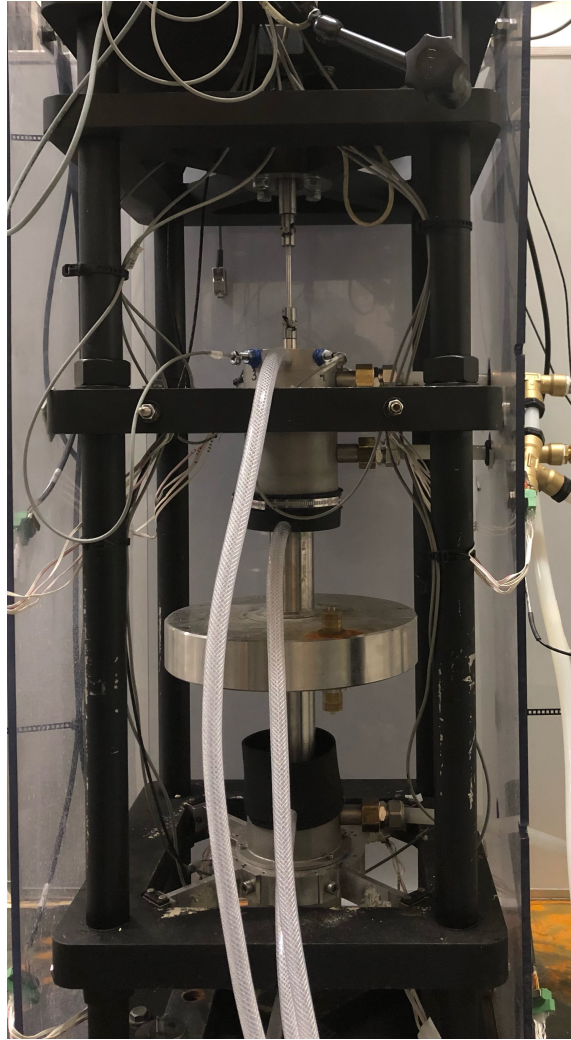

Figure 19: The rotor rig in Vattenfall's facilities in Älvkarleby.

The discretised structure and rotor are illustrated in Figure 20. 3932 eight noded tetrahedra (CTETRA8) elements were used for the structure. A total of 48 beam elements (CBEAM) compromise the pillars. The rotor disk comprises five beams, and ten beams per side compromise the shafts. Two CBEAR2 elements are used to model the bearings, which connect the bearing node to the structure by RBE2 elements. RBE3 elements were also used to connect the beam elements (of the structure's pillars) to the plates. The nodes of the bottom face of the model are fixed concerning all degrees of freedom. A non-structural mass of 6.76 kg is applied to the top plate to represent the top-mounted electric motor. The bearing nodes are fixed in the rotor axis translational direction, representing the axial constraint provided by the stinger coupling.
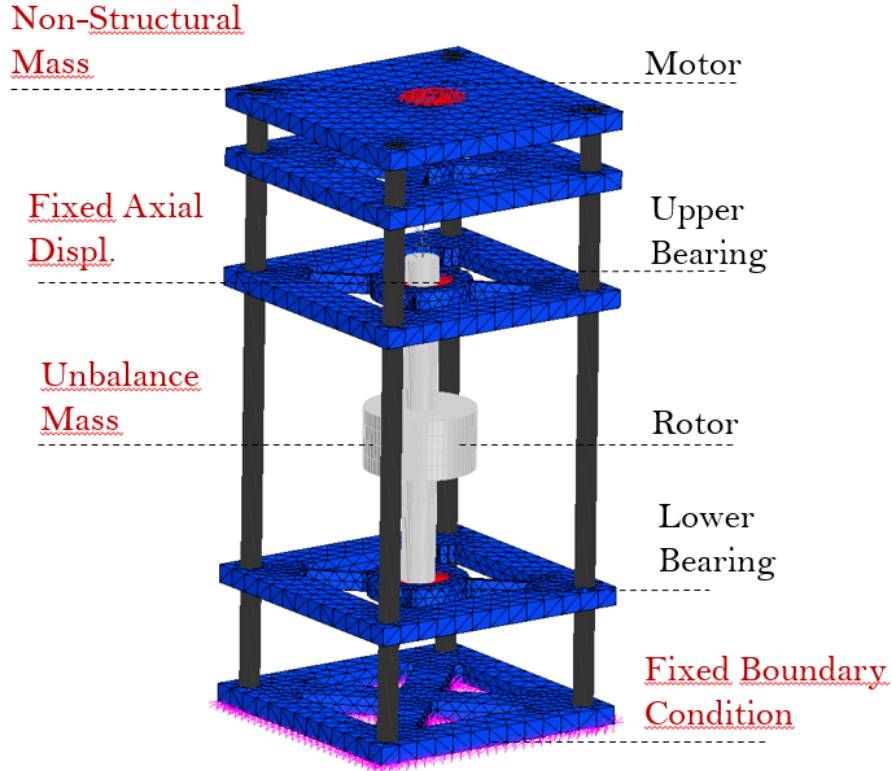

Figure 20: The discretised rotor rig.

The bearings of the system are simulated by the procedure outlined in Section 3.3. The local stiffness and damping matrices in Equations (28) and (29) are calculated by the use of Equations (34) and (35). The angular position and eccentricity of the bearing are given by Equations (37) and (38) for every time step during the simulation. After

computing the matrices in the rotating system, the transform outlined in Equation (32) is utilised based on the current angular position. The coefficients of the polynomial fit are found in Appendix A: Switch Routine Code, together with statistical parameters used for the rotor speed and eccentricity normalisations.

A constant rotor speed of 2000 rev/min is used for a four pad bearing simulation, with a radial bearing clearance of 0.13 mm. The unbalance mass of 80 g is applied at a radial distance of 70 mm. These parameters are provided in the Simcenter Nastran interface. The rotor speed is retrieved from the ROTORD-entry described in Section 3.6. The unbalance is specified on the mid-node at the geometrical centre of the rotor. The forces in the stationary coordinate system of the four pad bearing are shown in Figure 21b. A maximum deviation of approximately 20.8 % is noted for the forces in the y-direction, based on the difference between the mean value of the experimental data and the simulation. The maximum deviation in the x-direction is 9.8 %. The corresponding displacement orbit of the bearing is shown in Figure 21a. Results for an eight-pad bearing under the same operating conditions can be found in Appendix 2: Tilting 8-Pad Journal Bearing Results.
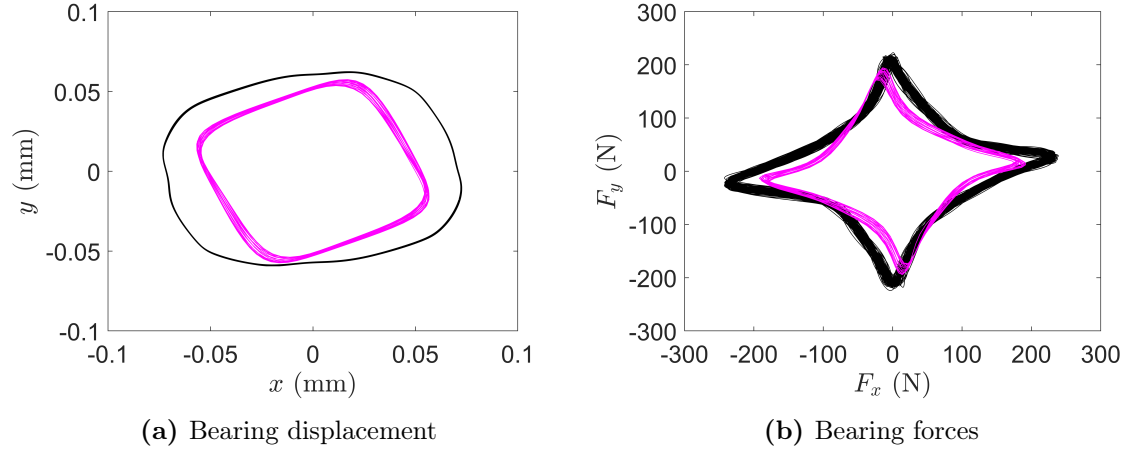

(a) Bearing displacement

(b) Bearing forces

Figure 21: Results for the four-pad tilting journal bearing in the stationary coordinate system at an unbalance of 0.0056 kgm and 2000 rev/min rotor speed. Experimental data are given in black and simulated data in colour.

The variation of the forces in the upper and lower bearings are presented in Figure 22, describing the difference between lower and upper force magnitudes. The lower bearing is exposed to higher forces on average. The difference is approximately 12 N at its maximum, representing about 6 % of the maximum forces in the simulation. A simulation time of 0.5 s was utilised with time step increments of 0.5 ms.
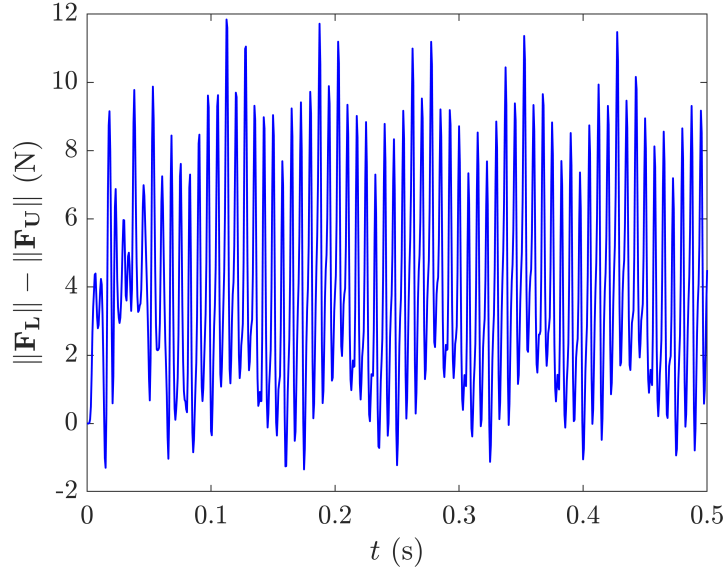
Figure 22: The difference in magnitudes between lower bearing force ($\mathbf{F_L}$) & upper bearing force ($\mathbf{F_U}$).

Due to the fixed boundary condition at the bottom end, the supporting structure exhibits higher *absolute* displacements at its free, upper end. This seems to reduce the *relative* displacements of the upper bearing, which directly yields lower forces. Nevertheless, due to the relatively high stiffness of the supporting structure, the observed deviations are marginal.

4.4 Analysis of a Hydropower Rotor Unit

To investigate if the critical rotor modes are extracted for a highly discretised rotor unit and provide insight into components which require 3D-finite element analysis, two different approaches were used to analyse hydropower rotor assembly: A three-dimensional solid element analysis in Simcenter Nastran's modal solver (SOL 414/110) and a *shaft-line model* by a beam-based finite element approach, conducted in Michael Friswell's open-source rotordynamic software for lateral vibrations in MATLAB R2021b [15]. The simulations aim to study how the dynamics of the rotor assembly are affected by the presence of a flexible rotor disk, e.g. the generator rotor ring, albeit with a heavily simplified geometrical model. The rotor geometry is an idealisation based on the now-defunct Porsi G1 hydropower assembly, previously located in the Lule älv outside of Vuollerim, Sweden. A simplified presentation of the hydropower unit is given in Figure 23.
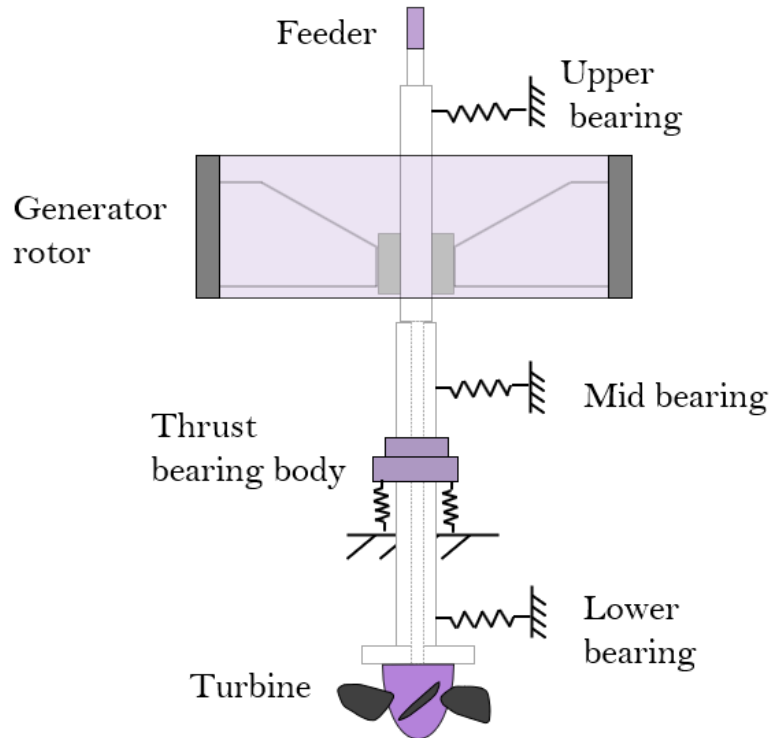

Figure 23: Illustration of the hydropower unit.

Both models assume a linear magnetic interaction between rotor and stator. No acceleration of gravity is considered and constant bearing stiffnesses are assumed. Inertial, stiffness and geometrical input data are presented in Table 7. The total mass of the whole rotor unit is about 500 tonnes, for which approximately 60% is attributed to the generator rotor ring.

Table 7: Inertia values for shaft line model and 3D model of the hydropower unit.

	Rotor Ring	Feeder	Body	Turbine
Mass (10^3 kg)	320	7.8	25.0	65.0
Diametral Inertia (10^3 kgm^2)	3150	47.3	246	639
Polar Inertia (10^3 kgm^2)	5200	24.7	410	1066

Undamped, isotropic bearings with constant stiffness are assumed for simplicity, which data is presented in Table 8. The negative magnetic stiffness $\mathbf{K_{MAG}}$ is computed according to Equation (40), with the scalar magnetic stiffness of -0.2 GN/m. $\mathbf{K_3}$ to $\mathbf{K_1}$ denotes the bearing stiffness matrices from highest to lowest.

Table 8: Stiffness values for shaft line model and 3D-model of the hydropower unit. The 4x4 matrix is symmetrical. Columns 1-2 and 5 are given in GN/m, 3-4 and 10 in GNm/rad, 6-7 in GN and 8-9 in GN/rad.

	k_{11}	k_{22}	k_{33}	k_{44}	k_{12}	k_{13}	k_{14}	k_{23}	k_{24}	k_{34}
$\mathbf{K_1}$	1.0	1.0	0.0	0.0	0.0	0.0	0.0	0.0	0.0	0.0
$\mathbf{K_2}$	1.0	1.0	0.0	0.0	0.0	0.0	0.0	0.0	0.0	0.0
$\mathbf{K_3}$	0.10	0.10	0.0	0.0	0.0	0.0	0.0	0.0	0.0	0.0
$\mathbf{K_{MAG}}$	-0.20	-0.20	-0.37	-0.37	0.0	0.0	-0.22	0.22	0.0	0.0

4.4.1 Shaft Line Model

The shaft-line model is illustrated in Figure 24, which encompasses twelve nodes and eleven beam elements, with node numbering from bottom to top. The shaft is isotropic steel with Young's modulus of 210 GPa, a density of 7850 kg/m^3 and Poisson's ratio 0.33. Due to its axisymmetry, the model is analysed in a stationary frame of reference.
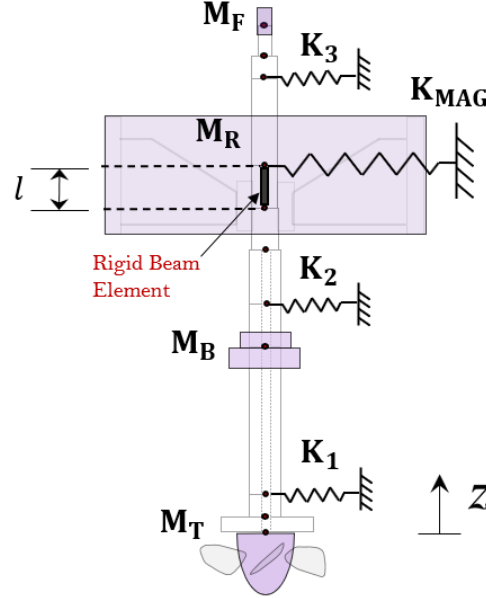

Figure 24: The shaft-line model of the Porsi G1 rotor unit. Components illustrated in purple are idealised as lumped masses, while beam elements model the parts in white. The auxiliary beam element is also highlighted.

The turbine, the feeder and the axial thrust bearing bearing body are idealised as masses with specific inertial properties, described in Table 7. The generator rotor is idealised as a rigid mass, albeit with a (negative) stiffness contribution which describes the magnetic pull caused by the electromagnetic rotor-stator interaction. The centre of mass of the generator rotor resides above its connection point to the shaft at a vertical offset distance ℓ. To model this situation, a beam element of negligible mass is used to join the hub connection node to a node located at the centre of mass of the generator rotor. This node serves as the location for the generator mass element and the magnetic pull. This adjustment aims to model the torque produced by the magnetic pulling force and amplified inertial contributions. The rotor connections

are provided by three bearings, represented by constant stiffness matrices. Note that the magnetic stiffness is also applied in the form of a bearing.

The Campbell diagram of the shaft-line model is presented in Figure 25, showcasing the range of 0-600 rev/min and 0-30 Hz. The model is analysed in the stationary frame of reference. Crossings with the 1Ω line indicate critical speeds.

Figure 25: The Campbell diagram of the line-shaft model with the influence of magnetic pull.
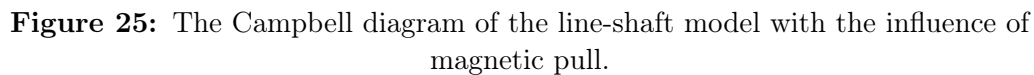
The Campbell diagram for the shaft-line model without magnetic pull is presented in Figure 26. The magnetic force lowers the system's total stiffness, resulting in a significant decrease of the first natural frequency pair from 3.7 Hz to 1.0 Hz, thereby reducing the first backward whirling critical speed from 190 to 35 Hz and the first forward whirling speed from to 360 to 120 Hz. Notably, the higher residing natural frequencies are less affected by the inclusion of magnetic pull.
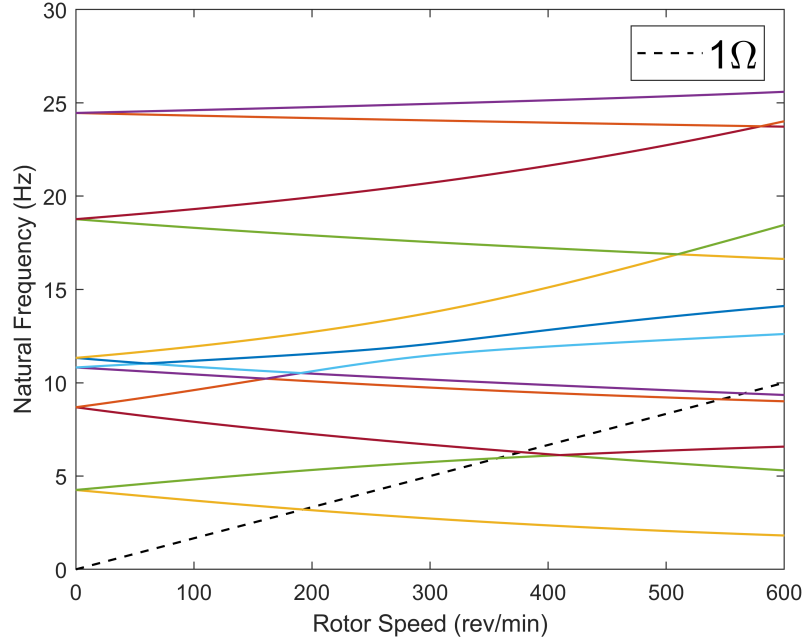
Figure 26: The Campbell diagram of the line-shaft model without magnetic pull.

The first four unique modes shapes of the shaft-line model (without considering magnetic pull) are presented in Figure 27, along with the corresponding natural frequency at 0 rev/min. The lower side is the turbine side.

Nat Freq = 3.7104Hz   Nat Freq = 7.4103Hz   Nat Freq = 9.9009Hz   Nat Freq = 10.8718Hz

Figure 27: Mode shapes from the shaft-line model without magnetic pull.

4.4.2 3D-Finite Element Model

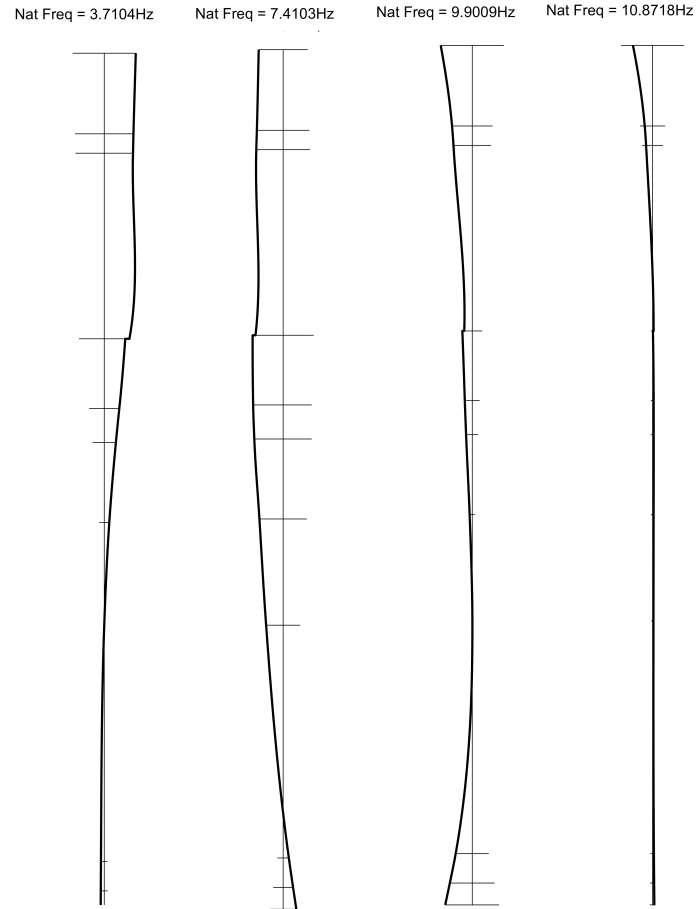A finite element model discretised by solid and shell elements is presented in Figure 28. The rotor ring (black) encompasses 22005 CHEXA8-elements and 2647 CQUAD8-shell elements. In total, the model covers approximately 400000 degrees of freedom. The shaft and plates (blue) are steel with Young's modulus of 210 GPa, a density of 7850 kg/m^3 and Poisson's ratio of 0.33. The data is also used for the rotor ring, albeit with a modified density of approximately 4000 kg/m^3 to obtain the correct mass and inertial properties.
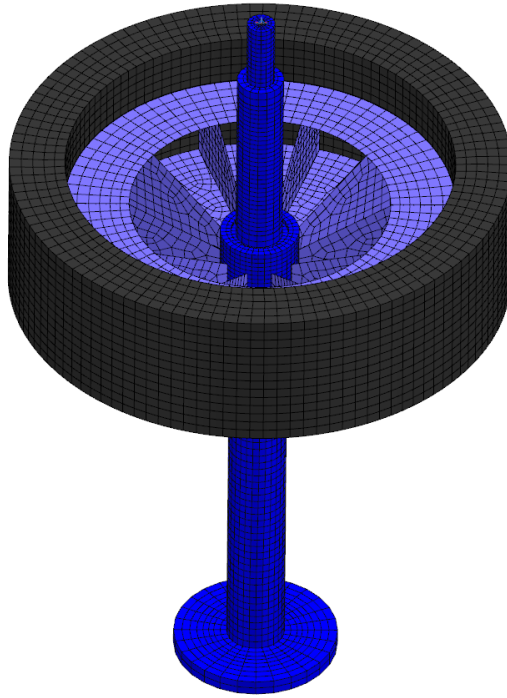
Figure 28: The 3D-finite element model of the Porsi G1 unit.

The model does not reflect that the physical generator ring is compromised of stacked steel plates. Instead, it is modelled as a continuum. Furthermore, the actual rotor spider utilises specific components to enable radial expansion due to centrifugal and temperature loads which are not modelled. CONM1-elements are used to model the external rotor components as lumped masses. The mass is applied to a single, central node on the rotor axis, connected to the cross-section by the use of RBE3-elements which are used to avoid excessive stiffening. The eigenvalue analysis was performed

in the rotating frame of reference due to non-axisymmetry caused by the rotor spider. As required in rotating frame analysis in Simcenter Nastran, a rotating load of 1 rad/s was applied to the whole model in a static subcase to compute the correct gyroscopic matrix.

The connection between the shell elements (plates) and the solid elements (rotor ring) is made possible by the mesh glueing functionalities in Simcenter Nastran PrePost (EDGE TO SURFACE GLUING), which is a recommended procedure for joining dissimilar meshes, establishing a welded connection to achieve proper displacement and load transfer. All bearings are made by CBEAR2-elements, where individual entries for the 6x6 matrices are supported. The magnetic pull is modelled as a bearing, acting at a node located at the geometric centre of the rotor ring. Ideally, the stiffness shall be applied to the whole ring surface to represent the magnetic pulling sufficiently.

The Campbell-diagram of the 3D-model is given in Figure 29. A range of 0-35 Hz and 0-600 rev/min was used for the diagram. As the analysis was performed in the rotating frame of reference, the output frequencies are also expressed in the rotating frame. Crossings with the 2Ω-line for the increasing frequencies give the backward whirling critical speeds. The crossing with the 0Ω line - the horizontal axis - gives the critical forward whirling speeds. Twenty frequencies were requested for each rotor speed.
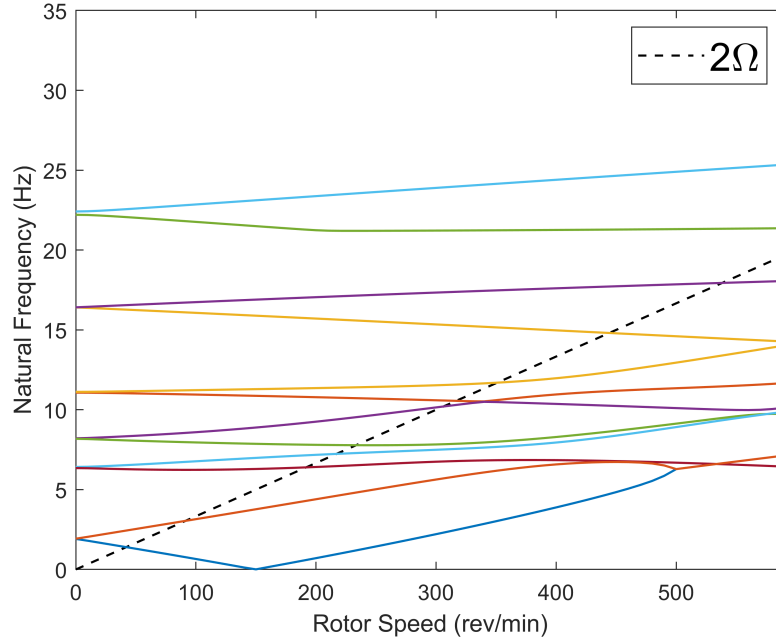

Figure 29: The Campbell diagram of the 3D-finite element model which shows natural frequencies in the rotating frame of reference. Magnetic pull included.

The Campbell diagram of the 3D-finite element model *without* magnetic pull is illustrated in Figure 30, showing the 0-35 Hz and 0-600 rev/min range. Once again, the magnetic pull lowers the system's total stiffness, resulting in a significant decrease of the first natural frequency pair from 3.5 Hz to 1.9 Hz, thereby lowering the first backward whirling critical speed from 160 to 100 Hz and the first forward whirling speed from to 290 to 150 Hz. Notably, the magnetic interaction affects the higher residing natural frequencies considerably less.
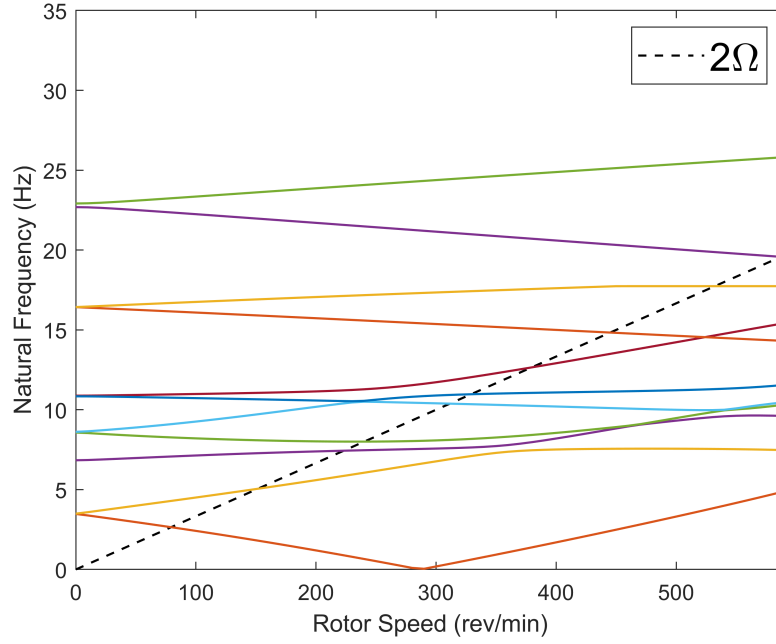
Figure 30: The Campbell diagram of the 3D-finite element model showcasing natural frequencies in the rotating frame of reference. No magnetic pull included.

The identified critical modes of the 3D-finite element model *without* magnetic pull
are illustrated in Figure 31, shown in the post-processing environment of Simcenter
Nastran. Tilting of the rotor ring is apparent for the first three mode shapes.
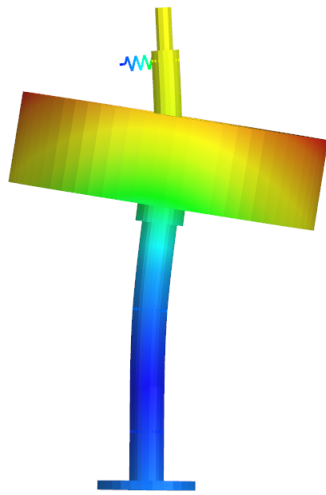
(a) First mode (3.5 Hz)
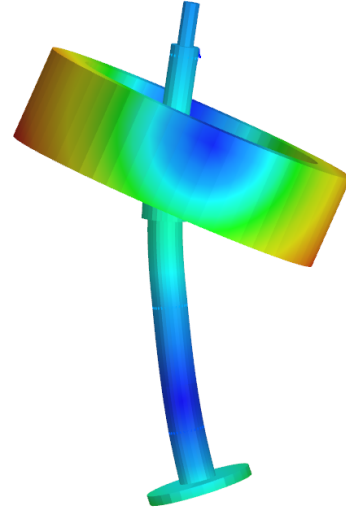
(b) Second mode (6.8 Hz)
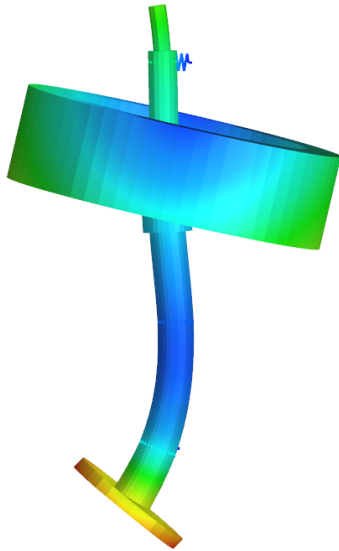
(c) Third mode (8.6 Hz)
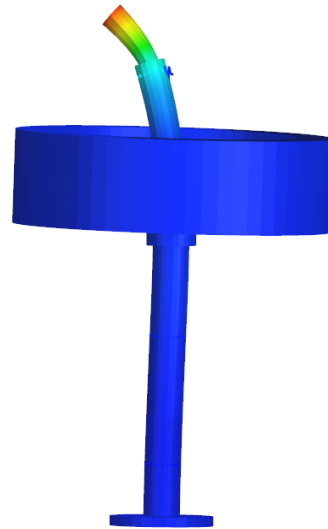
(d) Fourth mode (10.9 Hz)

Figure 31: Rotor vibration modes for the 3D-finite element model.

One of the non-critical modes is visualised in Figure 32, which is an expansion mode of the rotor ring. These frequencies are not deemed essential and have been removed from the Campbell diagrams to declutter the presentation. It is noted that similar auxiliary modes have little or no speed dependency in the Campbell diagram, enabling easy identification.
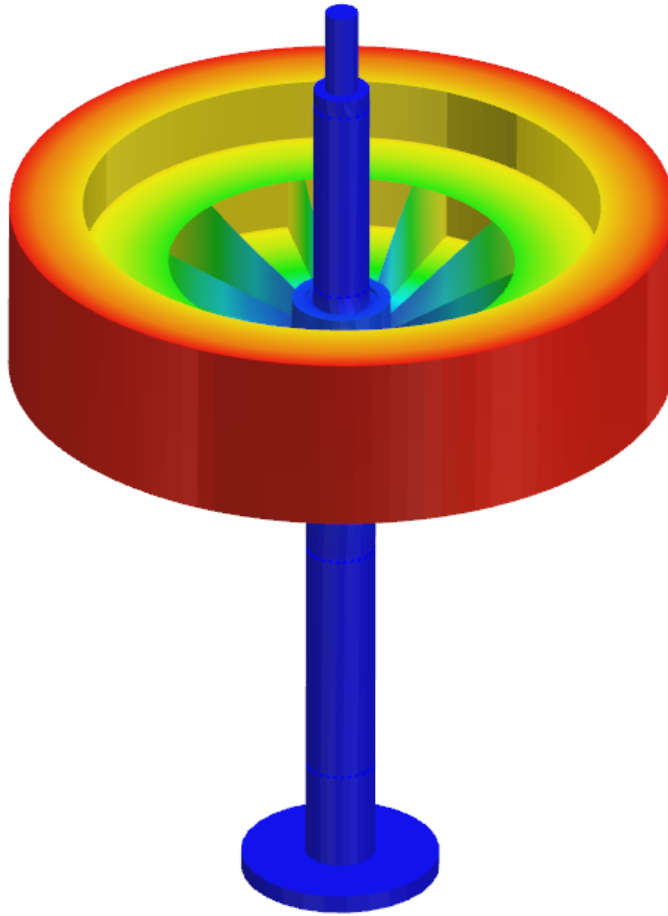
Figure 32: Expansion mode of the rotor ring at 5.0 Hz. No magnetic pull included.

By adjusting the ratio $\psi = E_R/E_S$, where E_R is Young's modulus for the ring and rotor spider and E_S is Young's modulus of the shaft, the first four static natural frequencies can be compared for different elasticity ratios. The result is presented in Figure 33. Note that the magnetic pull is not included in this study to reduce the involved variables. The horizontal dashed lines mark the natural frequencies found by the shaft-line model, which assumes that $\psi = \infty$.
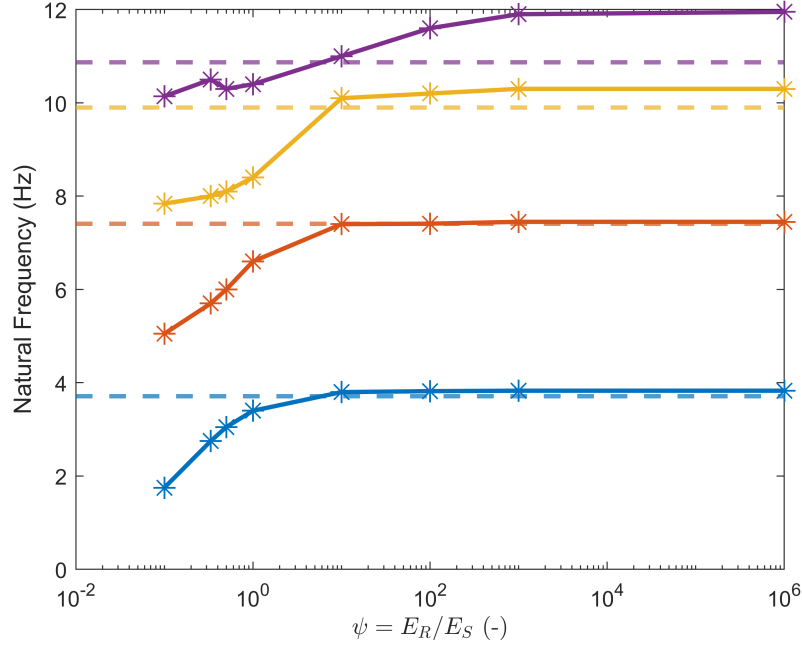
Figure 33: The static natural frequencies of the system as a function of the ring/shaft elasticity.

As observed, the lower range natural frequencies approach the shaft line model's frequencies with increasing stiffness of the rotor ring. For a rigid generator rotor, the deviation is highest for the highest frequency, which is about 10%. The lowest natural frequency shows a deviation of around 8.2% for a ratio of $\psi = 1$. For $\psi = 10^6$, this deviation is lowered to 2.6%. Noticeable discrepancies appear for $\psi < 1$, which underlines the limitations of the shaft-line model.

4.4.3 Discussion

The results underline differences in the presented models. The 3D-finite element model's first four mode pairs start at 3.5 Hz, 6.8 Hz, 8.6 Hz, and 10.9 Hz for the study without magnetic interaction. The shaft-line model's pairs start at 3.7 Hz, 7.4 Hz, 9.9 Hz and 10.9 Hz. Aside from the static frequencies, the diagrams are troublesome to compare visually, as they are produced in different frames of reference. The first two predicted critical speeds are similar; the shaft line model predicts the first backward critical speed at around 190 rev/min, whereas the 3D model predicts its occurrence at approximately 160 rev/min. The first forward critical speed occurs around 360 rev/min for the shaft line model and 300 rev/min for the 3D-FE model. Furthermore, all frequencies are lower for the 3D model, suggesting lower stiffness of the entire rotor assembly. It is inspected that the models' mass and inertial properties are within ±5%, but the stiffness is unfortunately not as straightforward to compare. Furthermore, finer discretisation or higher-order elements do not reduce the deviation between the models.

The first four mode shapes of the models share similarities in both form and frequency, which suggests that the critical rotor modes have been identified for the system. The auxiliary beam element in the shaft-line model introduces local distortion in the mode shapes, located at the placement of the generator rotor. Deviation for the forms is expected due to the vibration of the rotor ring. The excessive tilting movement of the rotor ring for the second mode is naturally only present for the 3D model and may not reflect the actual behaviour of a generator rotor, and could result from the connection procedure between the shell and solid elements that occur between the rotor spider plates and its hub.

The offset of the generator rotor demands special attention for both the system's inertia and for including magnetic pull, which imposes an additional torque due to the offset. The 3D model is assumed to describe these situations with more accuracy. The auxiliary beam element seems to yield adequate correspondence to the results of the 3D model, but more analysis must be done to verify that it can be used as a general procedure for modelling of centre-of-mass offsets, due to the fact that the 3D model is not validated. Furthermore, it must be noted that "layering" of beam elements represents a highly non-standard procedure in the beam based software and is far from a verified or explicitly supported method.

The magnetic pull effectively reduces the system's stiffness for both models, most distinctly for the first modes. However, it is also observed that the deviation for

the lowest frequencies is amplified to about 72%. Therefore, the most reliable conclusions for the model comparisons are done without inclusion of the magnetic pull. This suggests different interpretations of the magnetic stiffness between the models, raising questions regarding the validity of this subcategory of results. Indeed, the magnetic force is only applied on the rotor ring centre node in the 3D model - a more accurate representation would be a surface-based load, acting as a function of the ring displacement. The possibility of this was not researched in detail during the thesis and remains an appreciable task for further work.

The discrepancy between the models suggests that the flexible rotor ring alters the system's dynamics. As shown in Figure 33, notable differences occur for low elasticity ratios. This certainly makes a case for the 3D-finite element modelling approach, suggesting that high-mass, elastic rotor disks should be prioritised for the analysis. As a final note, it is not apparent which model provides the best description for the rotor behaviour, and experimental validation must be done to draw further conclusions.

5   Conclusions

The tilting pad journal bearing analysis shows that user-written bearing formulations can be implemented in Simcenter Nastran, enabling the user to replicate arbitrary bearing properties. An intricate external structure can be implemented in the analysis, underlining the possibility of studying stator/rotor interaction. This interaction can lead to interesting phenomena, as highlighted in the bearing force comparison. Thus, 3D-finite element modelling is an appropriate option when this interaction is assumed to be influential and when the stator's stiffness cannot be reduced to a one-dimensional representation.

The element comparison of the mid-span Jeffcott rotor shows that 3D elements should be limited to intricate geometry, e.g. non-axisymmetric or complex rotor components, which effectively decreases the computational effort. For example, an axisymmetric shaft is perfectly represented as a beam element, which effectively reduces the total degree of freedom of the model. The 2D-Fourier elements are an efficient alternative for modelling a wide range of axisymmetric rotors, achieving computational efficiency without compromising accuracy. It should be noted that even though the element formulation is axisymmetric, displacements and loads do not adhere to that limitation. Combinations between element types are also supported and can be utilised if necessary, i.e. to connect a complicated rotor disk by 3D elements to a uniform, axisymmetric shaft by 1D-beam elements.

The study of the two models for the hydropower unit underlines a situation where 3D-finite element modelling may be the only option for accurate analysis. The fundamental question is if a rotor component can be considered flexible or rigid with respect to the shaft or bearings, which is especially important if the component represents a high percentage of the rotor assembly mass. This assumption can significantly change the natural frequencies of the studied system. The results suggest that a high mass, flexible rotor disk significantly alters the hydropower unit's dynamical properties, which beam based rotor models cannot capture. Nevertheless, it must be emphasised that it is not apparent which model holds the most accurate description of the actual rotor behaviour, and tests must be done to validate the results. The mode extraction in the high-DOF system was performed adequately: Critical vibration modes were identified, with shapes similar to the shaft-line model. Non-critical modes (e.g. expansion modes) are easily identified and separated from the Campbell diagram.

In conclusion, finite element modelling in three dimensions provides a feasible alternative for modelling complex rotor dynamic assemblies, where rotor/stator interaction is critical for the dynamic characteristics or when elastic rotor components influence the dynamics of the whole rotor assembly. To pinpoint exactly when these conditions occur is a delicate matter and must be preceded by experiments, experience or simulations. The highly discretised 3D analysis is undeniably more computationally demanding and expensive than the beam based approach. Still, modelling techniques such as super element reduction can condense high-DOF rotors assemblies to substantially more compact models [16]. Nevertheless, as a general conclusion regarding advanced modelling techniques, it is highly recommended to verify the complex rotor models with the lumped parameter models to get a picture of the system's dynamic characteristics. Thus, the 3D-finite element approach shall be considered as a complement to the lumped parameter models and not as a perfect replacement.

References

[1] Energimyndigheten. *An overview of Energy in Sweden 2021*. Accessed on 2022-03-10. 2021.

[2] Paul Waide and Conrad Brunner. *Energy-Efficiency Policy Opportunities for Electric Motor-Driven Systems*. Accessed on 2022-03-10. 2011, p. 11. ISBN: 978-91-7993-020-2.

[3] Agnieszka Musyńska. *Rotordynamics*. Taylor & Francis Group, 2005. Chap. Preface, p. 1.

[4] Michael Friswell et al. *Dynamics of Rotating Machines*. Cambridge University Press, 2010. Chap. Finite Element Analysis of Rotors with Deformable Cross Sections, p. 431.

[5] Michael Friswell et al. *Dynamics of Rotating Machines*. Cambridge University Press, 2010. Chap. Free Response of Complex Systems, pp. 198–199.

[6] Michael Friswell et al. *Dynamics of Rotating Machines*. Cambridge University Press, 2010. Chap. Complex Rotor Models, p. 251.

[7] Michael Friswell et al. *Dynamics of Rotating Machines*. Cambridge University Press, 2010. Chap. Appendix 2: Stiffness and Mass Coefficients for Certain Beam Systems, pp. 500–501.

[8] Erik Elfgren. *Fysika - Tabell of Formelsamling i Fysik*. 2018, 3 and 21.

[9] Gudeta Berhanu Benti et al. "Numerical and experimental study on the dynamic properties of a four-pad and eight-pad tilting pad journal bearings in a vertical rotor". In: (2021), pp. 39–42.

[10] *ATAN2 — Arctangent function*. Accessed on 2022-05-06. URL: https://gcc.gnu.org/onlinedocs/gfortran/ATAN2.html.

[11] Rolf Gustavsson and Jan-Olov Aidanpää. "The Influence of Magnetic Pull on the Stability of Generator Rotors". In: (2004), p. 4.

[12] Michael Friswell et al. *Dynamics of Rotating Machines*. Cambridge University Press, 2010. Chap. Free Lateral Response of Simple Rotor Models, p. 103.

[13] *Rotor Dynamics Analysis (SOL 414)*. Accessed on 2022-02-05. URL: https://docs.sw.siemens.com/en-US/product/289054037/doc/PL20201105151514625.advanced/html/xid1757759.

[14] *Compile the .dll for proprietary bearing formulations (Linux)*. Accessed on 2022-03-29. URL: https://docs.sw.siemens.com/en-US/product/289054037/doc/PL20201105151514625.advanced/html/xid1969628.

[15]   *Dynamics of Rotating Machines.* Accessed on 2022-05-10. URL: http://www.rotordynamics.info/.

[16]   *Combine solution speed and accuracy for axisymmetric rotor dynamics.* Accessed on 2022-05-23. URL: https://blogs.sw.siemens.com/simcenter/combine-solution-speed-and-accuracy-for-axisymmetric-rotor-dynamics//.

Appendix A: Switch Routine Code

The switch routine (named MC750 for transient solver) is described here. This is based on a sample that is provided by the technical support from Siemens. The output bearing force (FORCE) is a 1x6 array. The function uses 1x6 array inputs in bearing positions U and velocity UD, and calculates the angular position of the rotor in the $[-\pi, \pi]$-range. Two entries are used that must be provided inside the Simcenter Nastran environment: the number of pads in CAG(1,2) and the radial clearance in variable CAG(2,2). These are provided as the input for a user written bearing function, and is given in the input meny for the CBEAR2 element.

```
      SUBROUTINE MC7520 (U,UD,UDD,FORCE,SKU,CU,SMU,NOP,NOEL,CAG,TIME,
     *                   ETIN,ETOU,ISYM,SS,NBRT,RGMPTR)
C Main function :
C
C               FUNCTION TO BE DEFINED BY THE USER :
C
C                 FORCE(6) = F (POSITONS,VELOCITIES)
C
C List of arguments:
C
C +-------+-------------------------------------------------+---+---+
C ! Name  ! Description                                     ! I ! O !
C +-------+-------------------------------------------------+---+---+
C ! NOEL  ! ELEMENT NUMBER                                  ! * !   !
C ! U     ! RELATIVE POSITIONS AND ROTATIONS (BUSHING AXES) ! * !   !
C ! UD    ! VELOCITY (TIME DERIVATIVE OF U)                 ! * !   !
C ! CAG   ! PROPERTY CODES 5001 TO 5250                     ! * !   !
C ! NOP   ! PRINTING OPTION (.DGE NOP4)                     ! * !   !
C ! TIME  ! TIME                                            ! * !   !
C ! ISYM  ! FLAG : NON SYMMETRICAL MATRIX (.DGE INLY)       ! * !   !
C !       !                                                 !   !   !
C ! FORCE ! FORCES AND TORQUES (BUSHING AXES)               !   ! * !
C ! SKU   ! STIFFNESS MATRIX   D(FORCE)/D(U)                !   ! * !
C ! CU    ! DAMPING   MATRIX   D(FORCE)/D(UD)               !   ! * !
C ! ETIN  ! STATE VECTOR AT PREVIOUS CONVERGED TIME STEP    ! * !   !
```

```
C ! ETOU  ! CURRENT STATE VECTOR                                    !   ! * !
C ! SS    ! VECTOR CONTAINING THE VALUES TO BE STORED (.SAE)  !   ! * !
C ! NBRT  ! NUMBER OF STORED VALUES (.SAE) - MAX. 100          !   ! * !
C +-------+----------------------------------------------------+---+---+
C
C======================================================================
C
!DEC$   ATTRIBUTES DLLEXPORT :: MC7520
      USE POINTER_DEFINITION
      IMPLICIT NONE
      INTEGER RGMPTR
      EXTERNAL RGMPTR

C Inputs
      DOUBLE PRECISION U(6),UD(6),UDD(6),FORCE(6),SKU(6,6),CU(6,6),
     *                 SMU(6,6),CAG(4,*),ETIN(6),ETOU(6),SS(100),OMEG,
     *                 NPADS
      INTEGER          NOP,NOEL,TIME,ISYM,NBRT,NSTEP,ITYP

C Local
      INTEGER          IUNIT,NBPT,NBPTMAX,I,J
      PARAMETER        (NBPTMAX=100)
      DOUBLE PRECISION ALPHA,EPS,EPS_PER,RADCLR,T(6,6)
      DOUBLE PRECISION :: PI = 3.14159265359
      DOUBLE PRECISION KMAXEE,KMINEE,KMAXNE,KMINNE
      DOUBLE PRECISION KMAXEN,KMINEN,KMAXNN,KMINNN
      DOUBLE PRECISION CMAXEE,CMINEE,CMAXNE,CMINNE
      DOUBLE PRECISION CMAXEN,CMINEN,CMAXNN,CMINNN
      DOUBLE PRECISION KEE,KNN,KNE,KEN
      DOUBLE PRECISION CEE,CNN,CNE,CEN

C     BETA, EE MAX

C     BETA, EE MIN

C     BETA, EN MAX

c     BETA, EN MIN
```

2

```
c     BETA, NE MAX

c     BETA, NE MIN

c     BETA, NN MAX

c     BETA, NN MIN

C     BETA, EE MAX

C     BETA, EE MIN

C     BETA, EN MAX

c     BETA, EN MIN

c     BETA, NE MAX

c     BETA, NE MIN

c     BETA, NN MAX

c     BETA, NN MIN

      CHARACTER*1000   TEXT
      DATA TEXT /' '/

      CALL MPTR(RGMPTR)

C COMPUTE ANGLE AND ECCENTRICITY
      ITYP = CAG(1,1)
      NPADS = CAG(1,2)
      RADCLR = CAG(2,2)
      ALPHA = ATAN2(U(2),U(1))

      EPS_PER = 100*sqrt(U(2)**2 + U(1)**2)/RADCLR
      EPS = (EPS_PER - 40.11)/25.89
```

```fortran
      OMEG = (30/PI*ETIN(4) - 1292)/803.5



C INITATE STIFFNESS, DAMPING AND TRANSFORMATION MATRICES
      DO J = 1,6
        DO I = 1,6
         SKU(I,J) = 0.0
         CU (I,J) = 0.0
         T(I,J) = 0.0
        END DO
      END DO

C CREATE TRANSFORMATION MATRICES
      T(1,1) = COS(ALPHA)
      T(2,2) = T(1,1)
      T(1,2) = SIN(ALPHA)
      T(2,1) = -T(1,2)
      T(3,3) = 1
      T(4,4) = 1
      T(5,5) = 1
      T(6,6) = 1

C Compute interpolation coefficients
          KMAXEE =
          KMAXEN =
          KMAXNE =
          KMAXNN =
          KMINEE =
          KMINNE =
          KMINEN =
          KMINNN =
          CMAXEE =
          CMAXEN =
          CMAXNE =
          CMAXNN =
          CMINEE =
          CMINEN =
          CMINNE =
```

```fortran
      CMINNN =



C Compute matrix coefficients

c Stiffness
      KEE = 0.5*(KMAXEE+KMINEE) + 0.5*(KMAXEE-KMINEE)*COS(NPADS*ALPHA)
      KEN = 0.5*(KMAXEN+KMINEN) - 0.5*(KMAXEN-KMINEN)*SIN(NPADS*ALPHA)
      KNE = 0.5*(KMAXNE+KMINNE) - 0.5*(KMAXNE-KMINNE)*SIN(NPADS*ALPHA)
      KNN = 0.5*(KMAXNN+KMINNN) - 0.5*(KMAXNN-KMINNN)*COS(NPADS*ALPHA)
c Damping
      CEE = 0.5*(CMAXEE+CMINEE) + 0.5*(CMAXEE-CMINEE)*COS(NPADS*ALPHA)
      CEN = 0.5*(CMAXEN+CMINEN) - 0.5*(CMAXEN-CMINEN)*SIN(NPADS*ALPHA)
      CNE = 0.5*(CMAXNE+CMINNE) - 0.5*(CMAXNE-CMINNE)*SIN(NPADS*ALPHA)
      CNN = 0.5*(CMAXNN+CMINNN) - 0.5*(CMAXNN-CMINNN)*COS(NPADS*ALPHA)



C Insert calculated values into matrices
c Stiffness matrix
      SKU(1,1) = KEE
      SKU(2,2) = KNN
      SKU(1,2) = KEN
      SKU(2,1) = KNE
c Damping matrix
      CU(1,1) = CEE
      CU(2,2) = CNN
      CU(1,2) = CEN
      CU(2,1) = CNE

      NBRT = 100


C Transform the matrices by the transformation matrix
      SKU = MATMUL(MATMUL(TRANSPOSE(T),SKU),T)
      CU = MATMUL(MATMUL(TRANSPOSE(T),CU),T)


C Compute bearing forces for output
      FORCE(1) = SKU(1,1)*U(1) + SKU(1,2)*U(2) + CU(1,1)*UD(1)
```

5

```
& + CU(1,2)*UD(2)
    FORCE(2) = SKU(2,2)*U(2) + SKU(2,1)*U(1) + CU(2,2)*UD(2)
& + CU(2,1)*UD(1)


 RETURN

 END
```

Appendix 2: Tilting 8-Pad Journal Bearing Results

With the same operating conditions as described in Section 4.3, an eight pad bearing was also simulated. The forces and displacements in the stationary coordinate system of the eight pad bearing are illustrated in Figure 34. Maximum deviations for forces are at 42 % and 27 % for the displacements, showcasing more than a double maximum deviation compared to the four-pad simulations. Furthermore, variations are most considerable in the positions between the pads, whereas on pad loading is more accurately described.
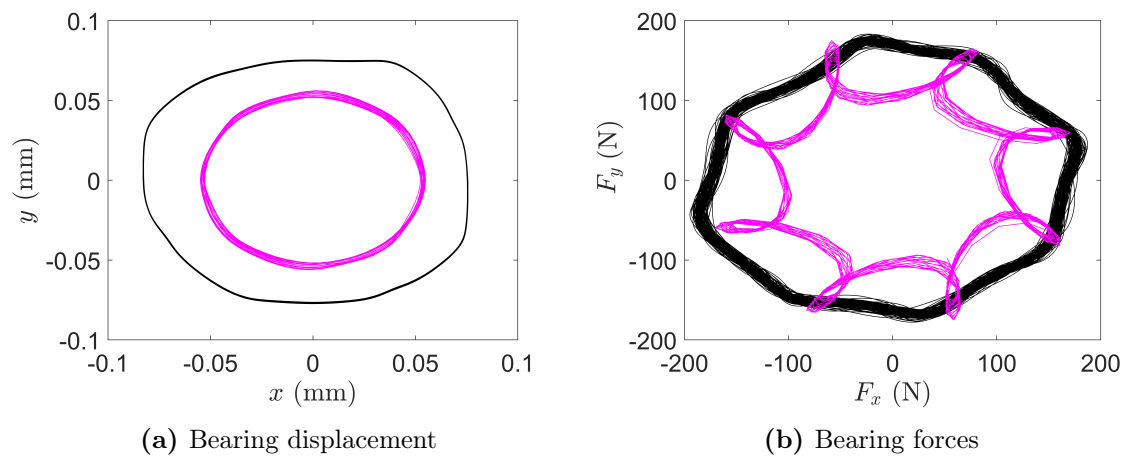

(a) Bearing displacement

(b) Bearing forces

Figure 34: Results for the eight pad tilting journal bearing in the stationary coordinate system at an unbalance of 0.0056 kgm and rotor speed 2000 rev/min. Experimental data are given in black and simulated data in colour.